Science Advances

AAAS

advances.sciencemag.org/cgi/content/full/2/6/e1501459/DC1

Supplementary Materials for

Edge-selenated graphene nanoplatelets as durable metal-free catalysts for iodine reduction reaction in dye-sensitized solar cells

Myung Jong Ju, In-Yup Jeon, Hong Mo Kim, Ji Il Choi, Sun-Min Jung, Jeong-Min Seo, In Taek Choi, Sung Ho Kang, Han Seul Kim, Min Jong Noh, Jae-Joon Lee, Hu Young Jeong, Hwan Kyu Kim, Yong-Hoon Kim, Jong-Beom Baek

Published 17 June 2016, *Sci. Adv.* **2**, e1501459 (2016)
DOI: 10.1126/sciadv.1501459

The PDF file includes:

Supplementary Materials and Methods

Materials. Graphite was obtained from Alfa Aesar (Natural, ~100 mesh, 99.9995% metal basis) used as received. Selenium (symbol: Se) was purchased from Aldrich Chemical Inc. (~100 mesh, ≥99.5% trace metals basis) and used as received. All other solvents were supplied by Aldrich Chemical Inc. and used without further purification, unless otherwise specified.

Instrumentations. The field emission scanning electron microscopy (FE-SEM) was performed on FEI Nanonova 230. The high-resolution transmission electron microscopy (HR-TEM) was performed on JEOL JEM-2100F microscope and atomic resolution transmission electron microscopy (AR-TEM) was carried out using Titan G2 60-300 microscope operated at the acceleration voltage of 80 kV. The TEM specimen were prepared by dipping carbon micro-grids (Ted Pella Inc., 200 Mesh Copper Grid) into well-dispersed samples in ethanol. Themogravimetric analysis (TGA) was conducted on a TA Q200 (TA Instrument) at a heating rate of 10 °C/min under air or nitrogen. The surface area was measured by nitrogen adsorption-desorption isotherms using the Brunauer-Emmett-Teller (BET) method on Micromeritics ASAP 2504N. X-ray photoelectron spectra (XPS) were recorded on a Thermo Fisher K-alpha XPS spectrometer. Elemental analysis (EA) was conducted with Thermo Scientific Flash 2000. X-Ray diffraction (XRD) patterns were recorded with a Rigaku D/MAZX 2500V/PC with Cu-Kα radiation (35 kV, 20 mA, $\lambda = 1.5418$ Å). Micro-Raman measurements were made with a WiTec Alpha300S system with 532 nm wavelength laser light and a 50 × objective.

Preparation of Electrodes. Homogeneously dispersed 0.1 wt.% sample powders in 2-propanol solution were obtained by ultrasonication for 30 min. The resultant solution was deposited directly onto on fluorine-doped SnO_2 (FTO)/glass (TEC-8, Pilkington) using an e- spray method. First, the sample dispersion solutions were loaded into a plastic syringe equipped with a 30-gauge stainless steel hypodermic needle. The needle was connected to a high voltage power supply (ESN-HV30).

A voltage of ~ 4.3 kV was applied between a metal orifice and the conducting substrate at a distance of 8 cm. The feed rate was controlled by the syringe pump (KD Scientific Model 220) at a constant flow rate of 70 μL min^{-1}. The electric field overcomes the surface tension of the droplets, resulting in the minimization of numerous charged mists. The resultant electrodes were sintered at 300 ^{o}C for 30 min at atmosphere prior to device fabrication. For the reference, the Pt-FTO electrode was also prepared by deposition of *ca.* 30 μL cm^{-1} of H_2PtCl_6 solution (2 mg of H_2PtCl_6 in 1 mL of ethanol) and sintered at 400°C for 15 min. The SEM images of the thin films of SeGnPs on fluorine-doped on FTO glass are shown in fig. S9.

Fabrication of Symmetrical Dummy Cells. Symmetrical sandwich-typed dummy cells were fabricated with two identical Pt- HGnP-, or SeGnP-FTO sheets, which were separated by 25-μm thick Surlyn (Solaronix, Switzerland) tape as a sealant and spacer leaving a 0.6 × 0.6 cm^2 active area. The sheet edges were coated by an ultrasonic soldering system (USS-9200, MBR Electronics) to improve electrical contacts. The electrolyte solution was prepared with 0.22 M $Co(bpy)_3(BCN_4)_2$, 0.05 M $Co(bpy)_3(BCN_4)_3$, 0.1 M $LiClO_4$, and 0.8 M 4-*tert*-butylpyridine (TBP), in acetonitrile. Co-complexes were prepared by reported procedure (*41*). Another iodine electrolyte solution was composed of 0.6 M 1,2-dimethyl-3-propylimidazolium iodide (DMPII), 0.1 M LiI, 0.05 M I_2, and 0.5 M TBP in acetonitrile. Electrolyte solution was introduced through a drilled hole on the CE *via* vacuum backfilling. The hole was sealed with cover glass using a Surlyn seal.

Electrochemical Analysis. All electrochemical measurements for electrocatalytic evaluation of materials were carried out with a *VersaSTAT* 3 (Version 1.31), AMETEK connected to a potentiostat at room temperature. The EIS spectra were acquired in the frequency range from 10^6 to 0.1 Hz, at 0 V of open circuit voltage, and the AC modulation amplitude was 10 mV. EIS data analysis was processed using the Zplot/Zview2 software.

Materials for DSSC Fabrication.

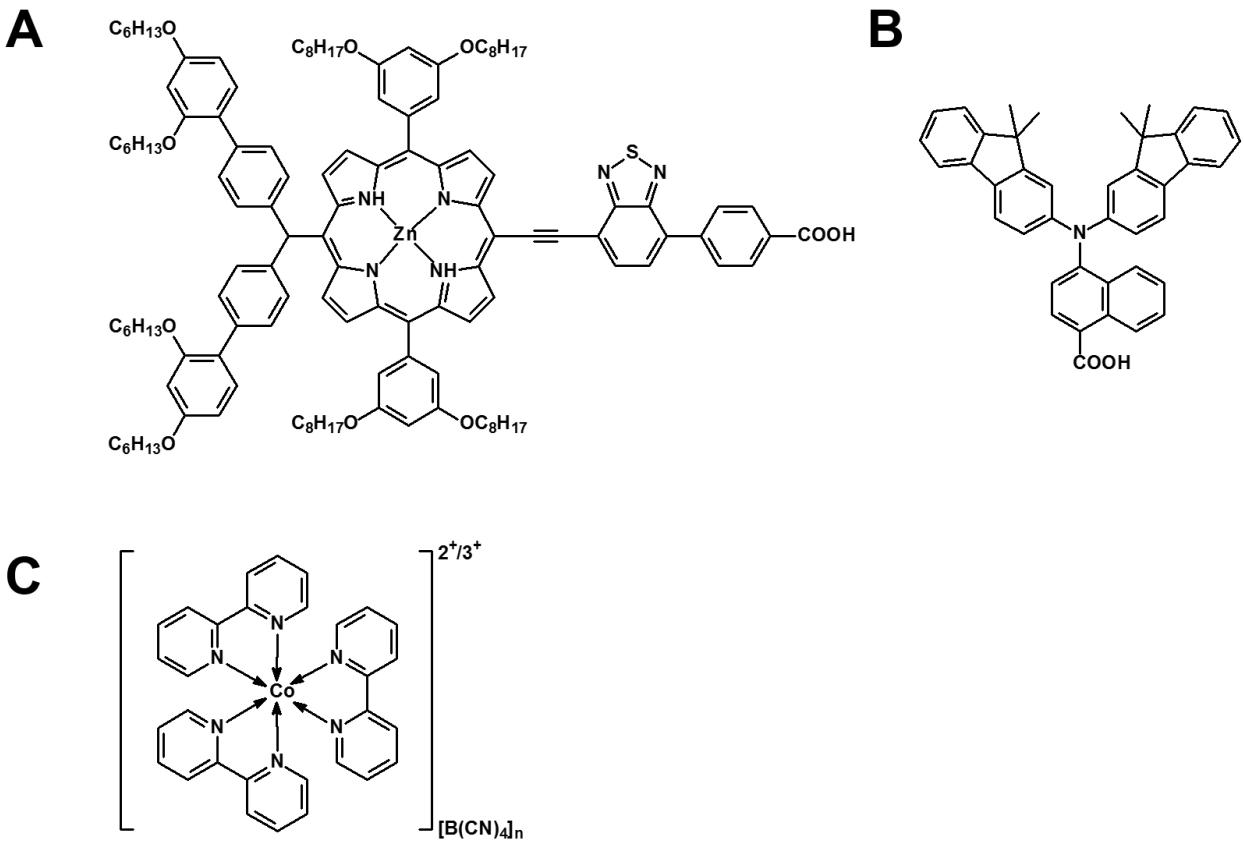

Chemical formulas. (A) SM315-sensitizer; **(B)** HC-A4 coadsorbent; **(C)** $Co(bpy)_3^{2+/3+}$ redox couple.

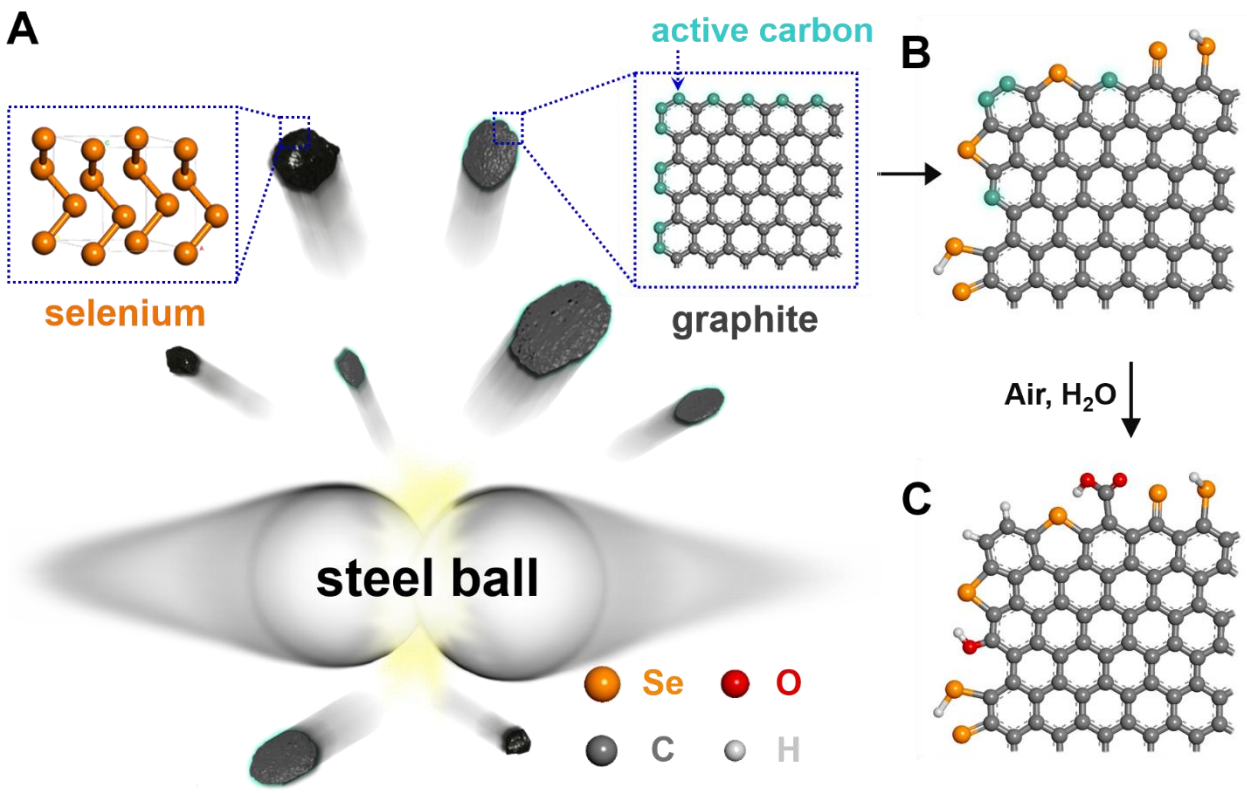

fig. S1. Schematic representation of mechanochemical ball-milling graphite in the presence of Se powder to produce edge-selenated graphene nanoplatelets (SeGnPs).

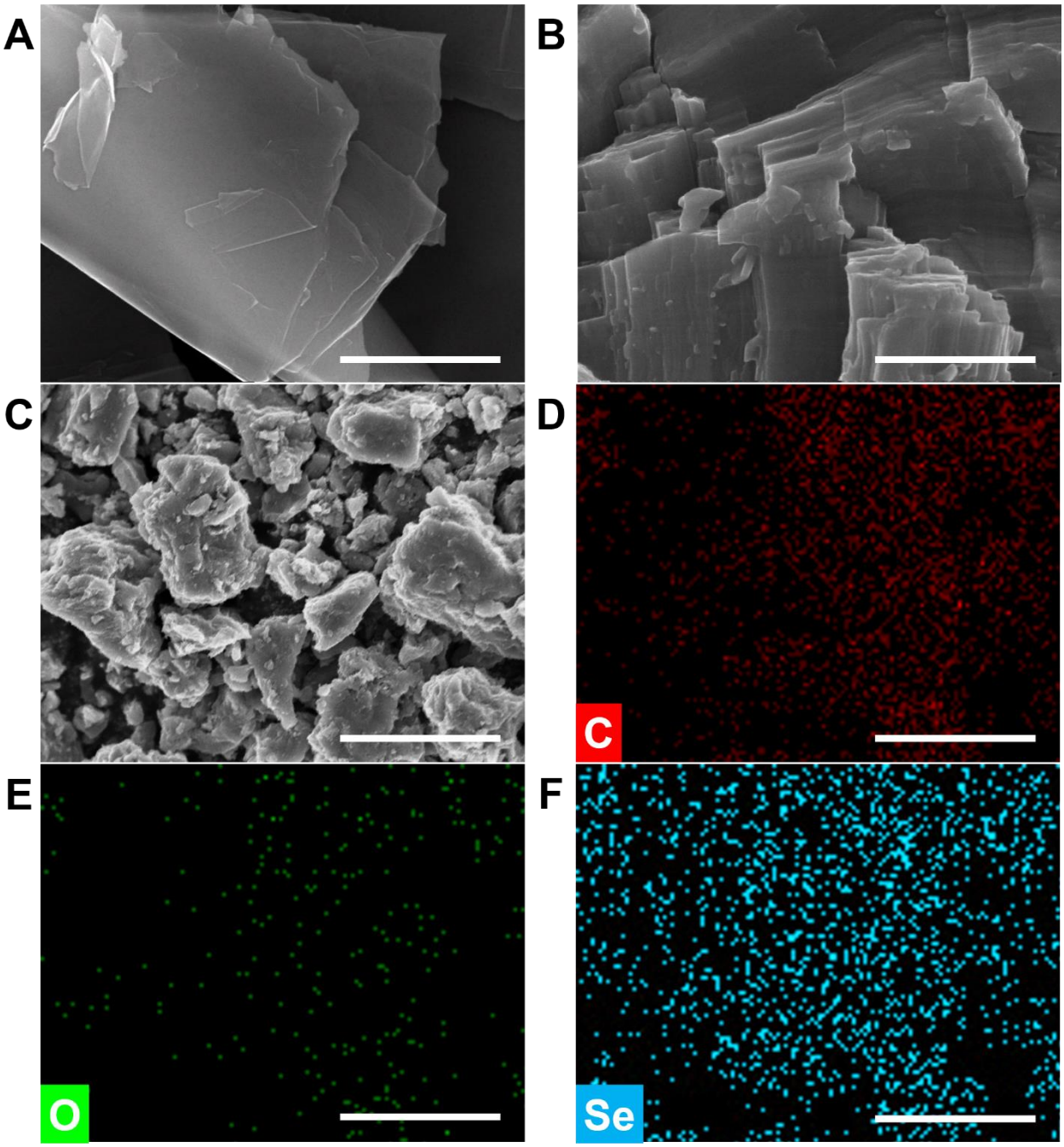

fig. S2. FE-SEM images: **(A)** The pristine graphite; (**B)** Selenium powder; **(C)** SeGnPs. Corresponding element mappings of SeGnPs: **(D)** Carbon; **(E)** Oxygen; **(F)** Selenium. Scale bars are 2 µm.

Scanning electron microscopy (SEM). As shown in fig. S2, scanning electron microscopy (SEM) images indicated that the pristine graphite has large grain size (< 150 μm, fig. S2A). However, after ball-milling graphite in the presence of selenium (Se, fig. S2B), the grain size of resultant SeGnPs was dramatically reduced to a few hundred nanometers (fig. S2C). The result implies that the mechanochemical reaction has occurred during ball-milling as follow: the unzipping of sp^2 C-C bonds in graphitic layers; the formation of active carbon species; subsequent reaction with Se to produce edge-selenated graphene nanoplatelets (SeGnPs). After complete work-up to remove free-standing Se, the presence of Se in SeGnPs was clearly evidenced by SEM energy dispersive X-ray spectroscopy (EDS) (fig. S4A) with element mapping (figs. S2D, S2E, and S2F). SEM-EDS indicated that the content of Se is approximately 5.57 at .% (table S1).

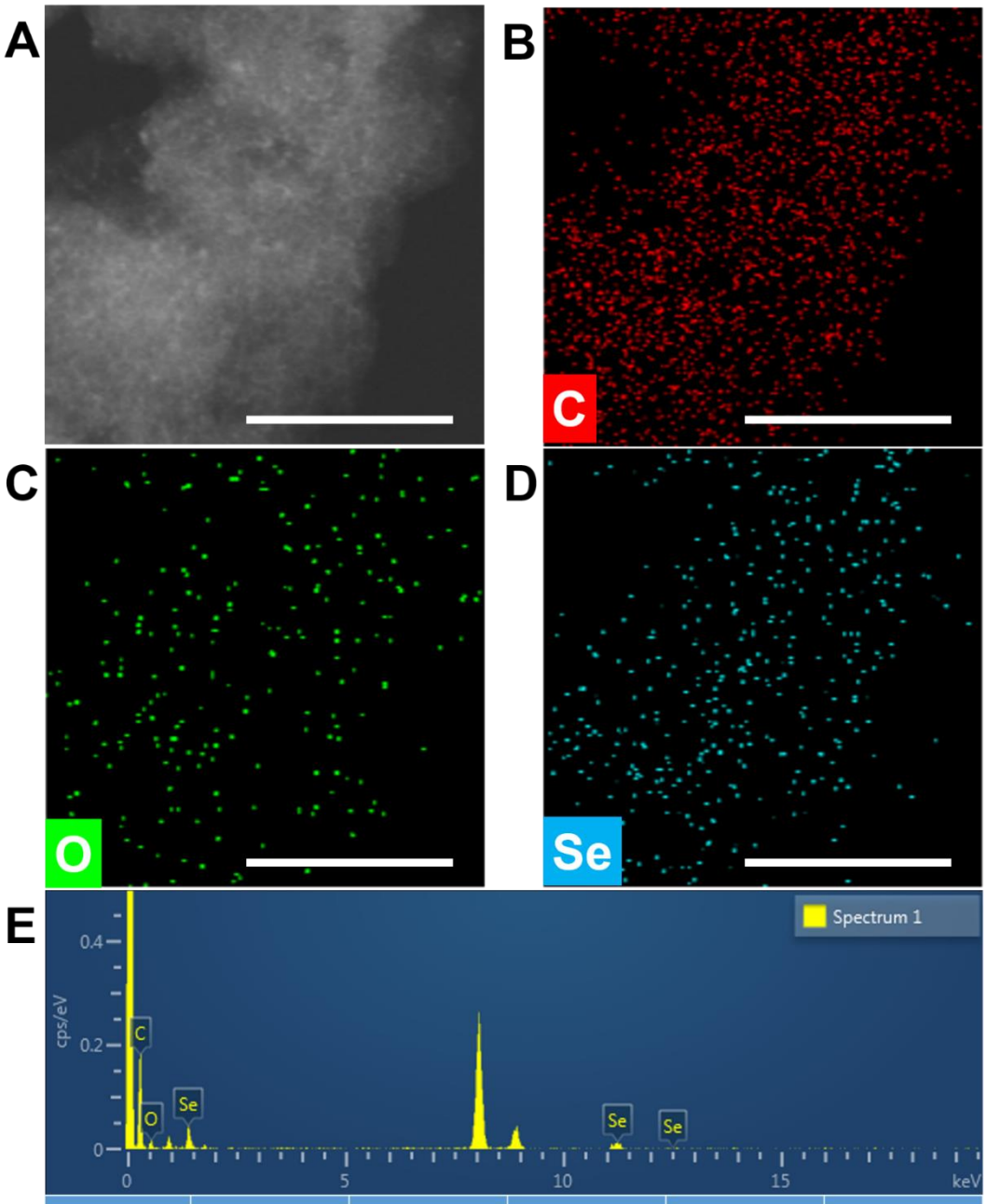

Element	Line Type	k factor	Absorption Correction	Wt%	Wt% Sigma
C	K series	2.75165	1.00	85.80	2.30
O	K series	2.00744	1.00	5.19	1.54
Se	K series	1.74684	1.00	9.02	1.81
Total:				100.00	

fig. S3. (A) Dark-field (DF) TEM image of SeGnPs. Corresponding element mappings: **(B)** Carbon; **(C)** Oxygen; **(D)** Selenium. Scale bars are 50 nm; **(E)** TEM energy-dispersive X-ray (EDX) spectrum of SeGnPs. The table shows corresponding element contents (wt.%).

Transmission electron microscopy (TEM). High angle annular dark field (HAADF) STEM images (figs. S3A and S3B) of SeGnPs clearly indicated that Se is attached as individual atom rather than aggregated cluster. Atomic-resolution TEM (AR-TEM) image of SeGnPs showed highly ordered structure with honeycomb lattice in the basal area and some distortion at the edge region (figs. 1B and S8A). The dark contrast (black arrow) is atomic Se. Furthermore, high-resolution TEM (HR-TEM) image shows that a number of black dots are observed along the edge lines of SeGnPs (black arrow in red box, fig. S8B) that can be strongly reminiscent of Se atoms, whose atomic radius is approximately 115 pm (carbon: 77 pm) (*42*). As a result, the mechanochemical reaction occurs only at the edges to form C-Se bonds and it preserves crystallinity at the basal plane, which is in agreement with edge-selective formation of C-Se bonds proposed in Fig. 1A.

High-angle annular dark field (HAADF) scanning TEM (STEM) image with element mappings clearly shows the presence of only atomic C, O and Se without impurities such as residual metals as well as free-standing Se particles (fig. S3). Furthermore, the corresponding Se content on SeGnPs from TEM EDS was 9.02 wt.% (fig. S3E).

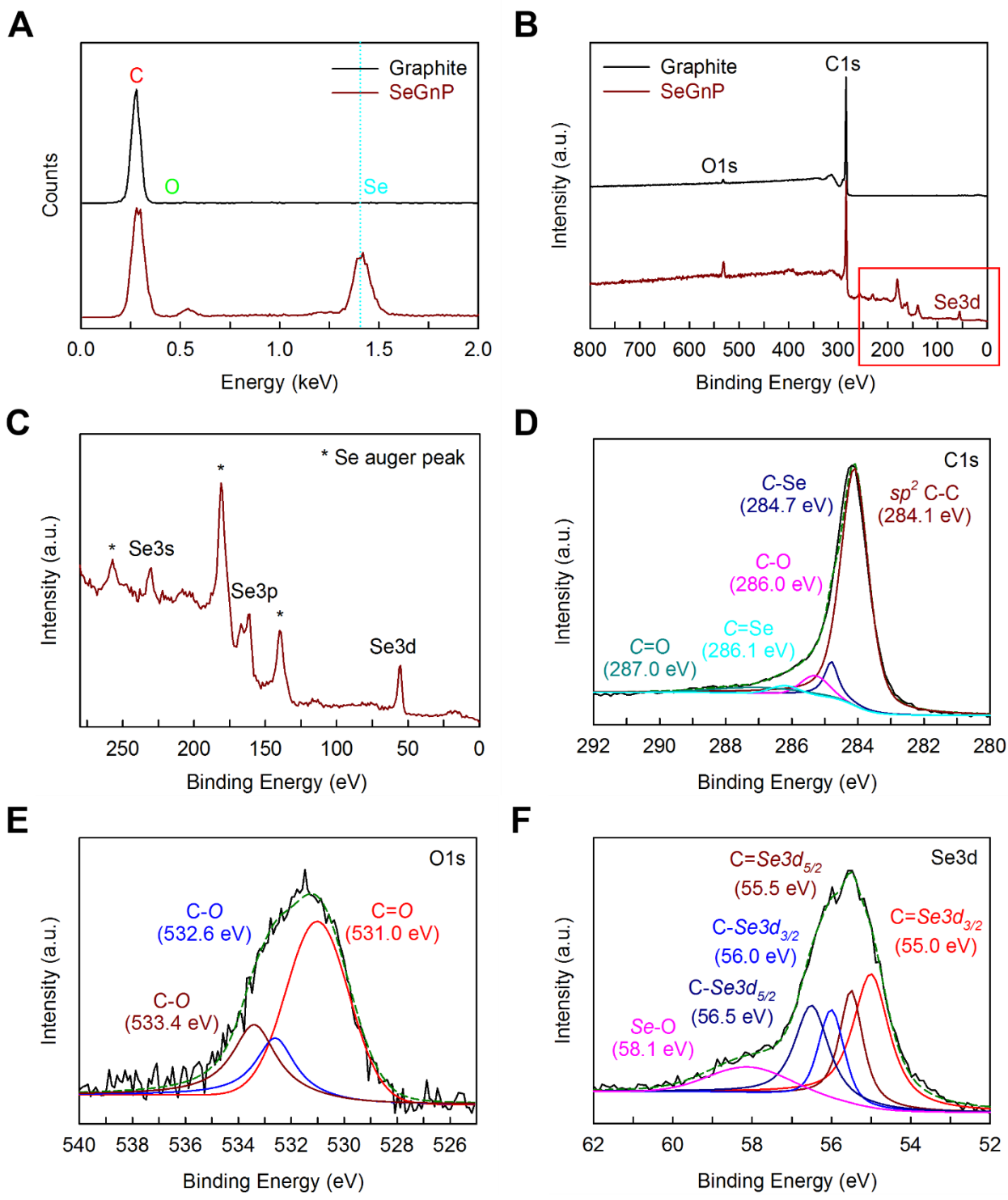

fig. S4. (A) SEM energy dispersive x-ray (EDX) spectra of the pristine graphite and SeGnPs. XPS spectra: **(B)** Full-scale survey spectra of the pristine graphite and SeGnPs; **(C)** Magnification of red box in fig. S4B. High-resolution XPS survey spectra of SeGnPs: **(D)** C 1s; **(E)** O 1s; **(F)** Se 3d.

X-ray photoelectron spectroscopy (XPS). X-ray photoelectron spectroscopy (XPS) was widely used for characterization of the chemical bonding state of the pristine graphite and SeGnPs (fig. S4C). The survey spectra of the pristine graphite show a main C 1s peak from sp^2 C-C bond along with a minor O 1s peak mostly related to physical absorption of oxygen and moisture (*43*) while SeGnPs show various Se peaks as well as C 1s and O 1s peaks, indicating that selenium was included in SeGnPs. Upon magnified red rectangle in fig. S4B, the SeGnPs show various Se signals such as Se 3s, Se 3p, Se 3d and auger electron signal of Se (fig. S4C) (*44*, *45*). The content of Se in SeGnPs is about 6.81 at.%, which is similar with SEM EDS result (5.57 at.%, table S1). High-resolution XPS spectra, together with the curve fittings and deconvolutions, showed that the C 1s peak of SeGnPs consisted of sp^2 C-C (284.1 eV), *C*-Se (284.7 eV) (*46*), *C*-O (285.3 eV), *C*=Se (286.1 eV) and *C*=O (287.0 eV) (fig. S4D) and O 1s peak of consisted of C=*O* (531.0 eV), Se-*O* (532.6 eV) and C-*O* (533.4 eV) (fig. S4E). The Se 3d spectrum exhibited C=$Se3d_{3/2}$ (55.0 eV), C=$Se3d_{5/2}$ (55.5 eV), C-$Se3d_{3/2}$ (56.0 eV), C-$Se3d_{5/2}$ (56.5 eV) and O-*Se* (58.1 eV) peaks (fig. S4F) (*47*, *48*), indicating the covalent C=Se and C-Se-C bonds at the edges of SeGnPs as schematically represented in Fig. 1A.

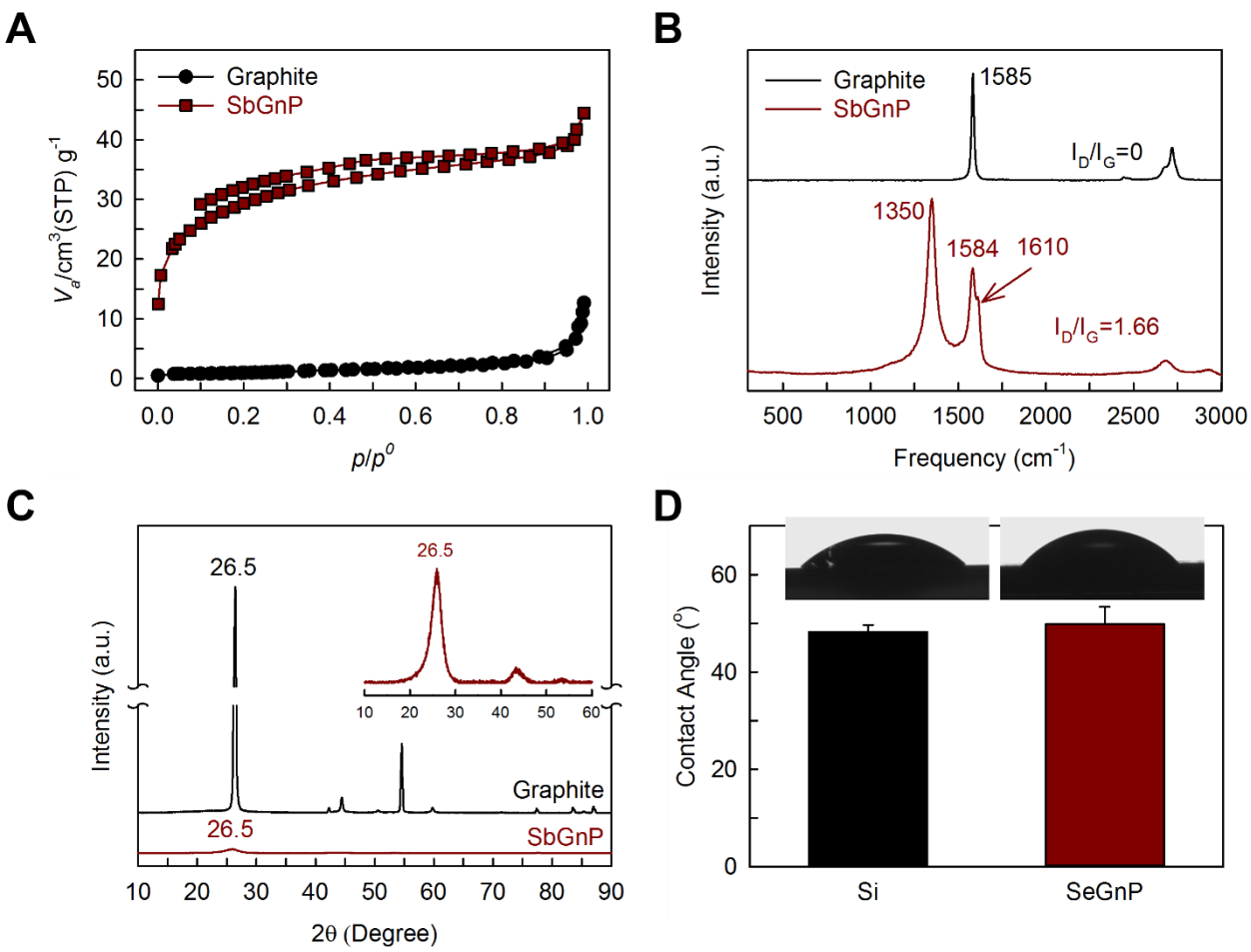

fig. S5. (A) Nitrogen adsorption-desorption isotherms of the pristine graphite and SeGnPs obtained at 77 K; **(B)** Raman spectra; **(C)** XRD diffraction patterns; **(D)** The average contact angles of silicon wafer and SeGnPs (inset: droplet images).

Brunauer-Emmett-Teller (BET), Raman, X-ray diffraction and contact angle measurements. The N_2 adsorption-desorption isotherms of the pristine graphite and SeGnPs are shown in fig. S5A. The Brunauer-Emmett-Teller (BET) specific surface area of the pristine graphite and SeGnPs was about 2.78 and 105.69 m^2 g^{-1}, respectively (table S2). Comparing with the pristine graphite, SeGnPs possessed much larger specific surface area (about 38.0 times) due to the delamination of graphitic layers *via* Se attachment at their edges. The sorption isotherm of SeGnPs belongs to a typical type-II, indicating that SeGnPs have macroporous and unrestricted monolayer-multilayer

(*49*). As a result, we can confirm that the pristine graphite was exfoliated in significant extend by selenium doping *via* ball milling and then graphitic layers are restacked as shown in SEM image (fig. S2C) in solid state.

The structures of the pristine graphite and SeGnPs were further studied using Raman spectroscopy (fig. S5B). The pristine graphite shows that only sharp G peak (1585 cm^{-1}) and low I_D/I_G ratio (~zero) due to large grain size (< 150 μm) and well-ordered graphitic structure. However, the G peak of SeGnPs was located at 1584 cm^{-1}, which is similar with the pristine graphite because of the preservation of sp^2 carbon structure. However, SeGnPs show a strong D peak (1350 cm^{-1}) and D' peak (1610 cm^{-1}, dark red arrow) with the I_D/I_G ratio of 1.66, due to the size reduction (see SEM image, fig. S2C) and edge-functionalization (*50*).

The degree of exfoliation in the solid state could be estimated by comparing X-ray diffraction (XRD) patterns (fig. S5C). The pristine graphite exhibits a strong and sharp [002] diffraction peak at $2\theta = 26.5°$, which correspond to well-ordered graphite interlayer distance of 0.34 nm (*51*). SeGnPs show negligibly low peak intensity (0.35 % compared to the pristine graphite) with the same [002] peak location at 26.5° (fig. S5C, inset), while graphite oxide (GO) that shows a large shift of the [002] peak at 10.5° (*52*). In the case of GO, the exfoliation of graphitic layers *via* random oxidation at both its basal area and edges. These results indicates the delamination of most graphitic layers *via* edge-selective Se-doping at the edges while preserving honeycomb lattice on basal area of SeGnPs during ball-milling and work-up procedures (see TEM images in Fig. 1B and fig. S8A).

After assuring the structures of SeGnPs, it investigated the polarity of SeGnPs through contact angle measurements. The average contact angle of silicon wafer as reference and SeGnPs was 48.3 and 49.3°, respectively (fig. S5D). Thus, although the electronegativity of selenium ($\chi = 2.55$) is same as carbon ($\chi = 2.55$) (*53*), a number of oxygenated functional groups helps the dispersion of SeGnPs via enthalpic contribution.

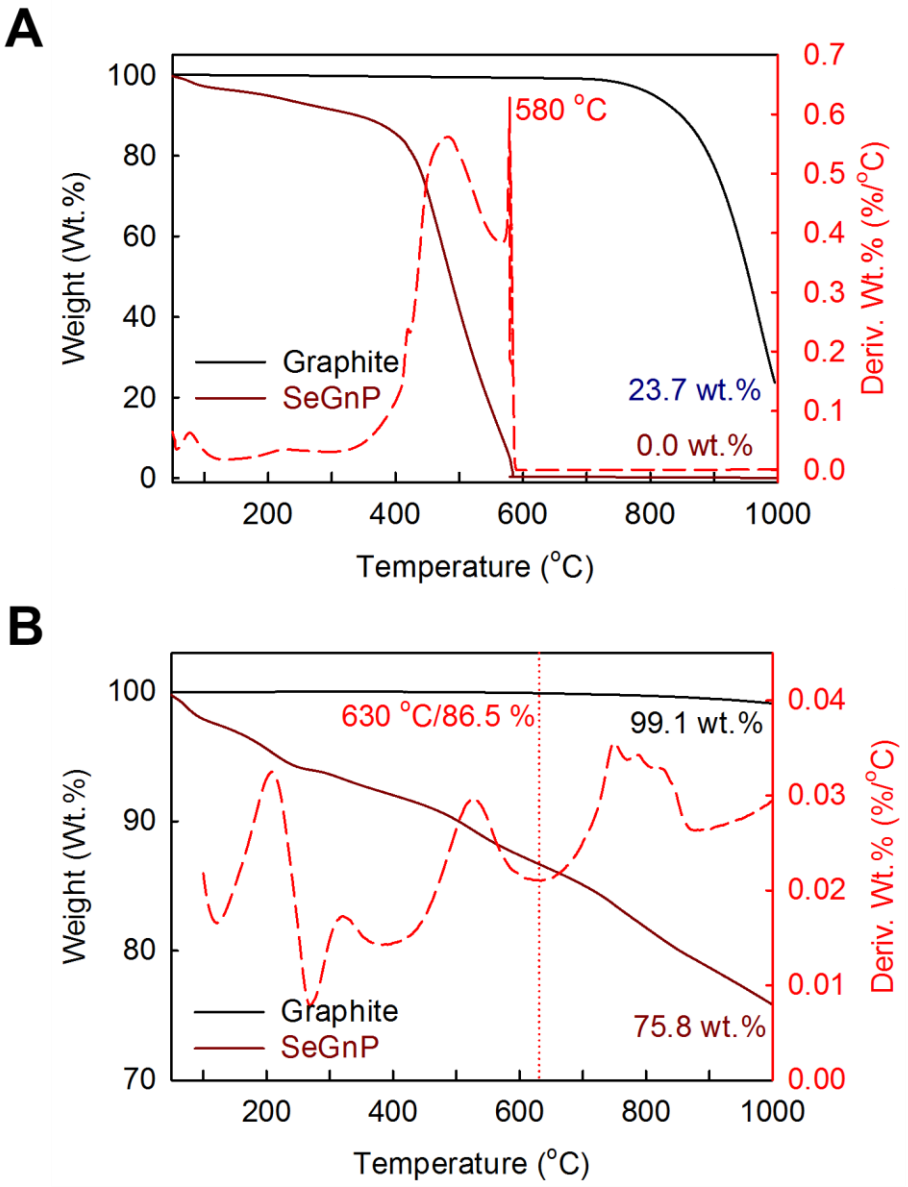

fig. S6. TGA thermograms of the pristine graphite and SeGnPs obtained at the heating rate of 10°C min^{-1}: **(A)** In air; **(B)** in nitrogen.

Thermogravimetric analysis (TGA). The char yields of the pristine graphite and SeGnPs at 1000 °C were 23.7 wt.% and 0.0 wt.% in air as well as 99.1 wt.% and 75.8 wt.% in nitrogen, respectively (fig. S6). The high thermal stability of the pristine graphite is due to its orderly structure and large grain size (< 150 µm, fig. S4A). However, SeGnPs displayed lower thermal stability than the pristine graphite because of very small grain size and a number of oxygen

containing function groups. In particular, SeGnPs displayed ~0 wt.% char yield above 600°C in air (fig. S6A). Considering boiling point (~685°C) of pure selenium (*54*), the physical state of selenium in SeGnPs is atomically attached to graphitic framework rather than free-standing Se clusters. This important result further supports TEM observation (Fig. 1B and fig. S8A), which suggests the atomic level distribution of selenium by C-Se bonds. In nitrogen atmosphere, TGA derivative curve shows few inflection points (fig. S6B). SeGnPs showed 13.5 wt.% weight loss up to 630°C, which is contributed bound moisture and oxygen containing functional groups such as -OH, -COOH, and -C=O that are formed during the termination of remnant carbon species by air constituents upon opening lid. The weight loss above 630°C is because of the decomposition of graphitic structure and dissociation of C-Se covalent bonds.

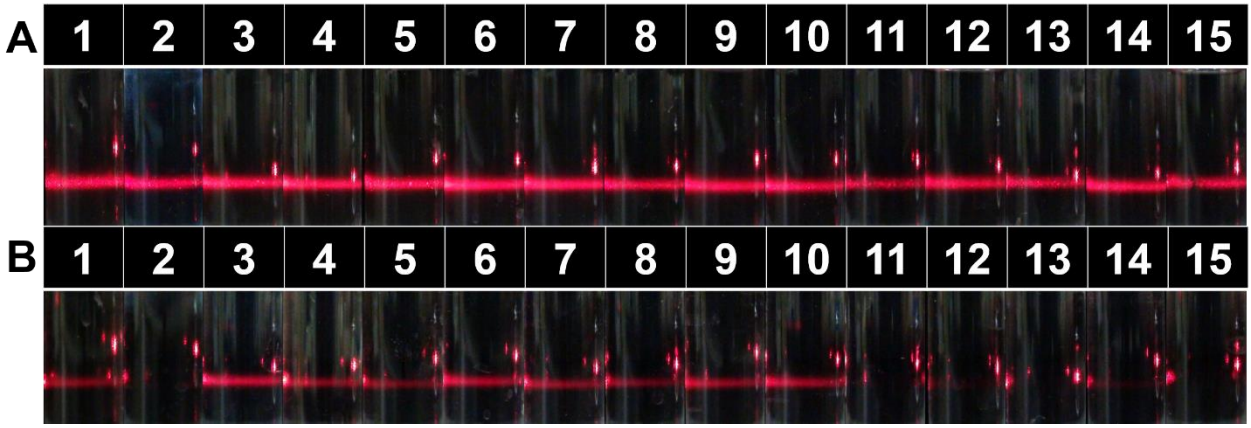

fig. S7. Photographs of SeGnPs dispersed solutions in various solvents on bench top in a normal laboratory condition: **(A)** After 30 seconds; **(B)** After 1 week. 1. H_2O; 2. 1 M HCl; 3. 1 M NH_4OH; 4. MeOH; 5. EtOH; 6. THF; 7. Acetone; 8. DMAc; 9. DMF; 10. NMP; 11. Toluene; 12. CH_2Cl_2; 13. Hexane; 14. Ethyl acetate (EA); 15. Diethyl ether.

Solubility. The increase of enthalpy and entropy via edge-functionalization (selenium and oxygen) and size reduction, respectively, can contribute to an efficient dispersion of SeGnPs in a various solvents (*55*). SeGnPs were found to be readily dispersible not only in polar protic solvents such as water, basic water, methanol and ethanol, but also in polar aprotic solvents including tetrahydrofuran (THF), acetone, *N*,*N*-dimethylacetamide (DMAc), *N*,*N*-dimethylformamide (DMF), *N*-methyl-2-pyrrolidone (NMP) (fig. S7), indicating that SeGnPs have an advantage for use in various applications *via* solution processing.

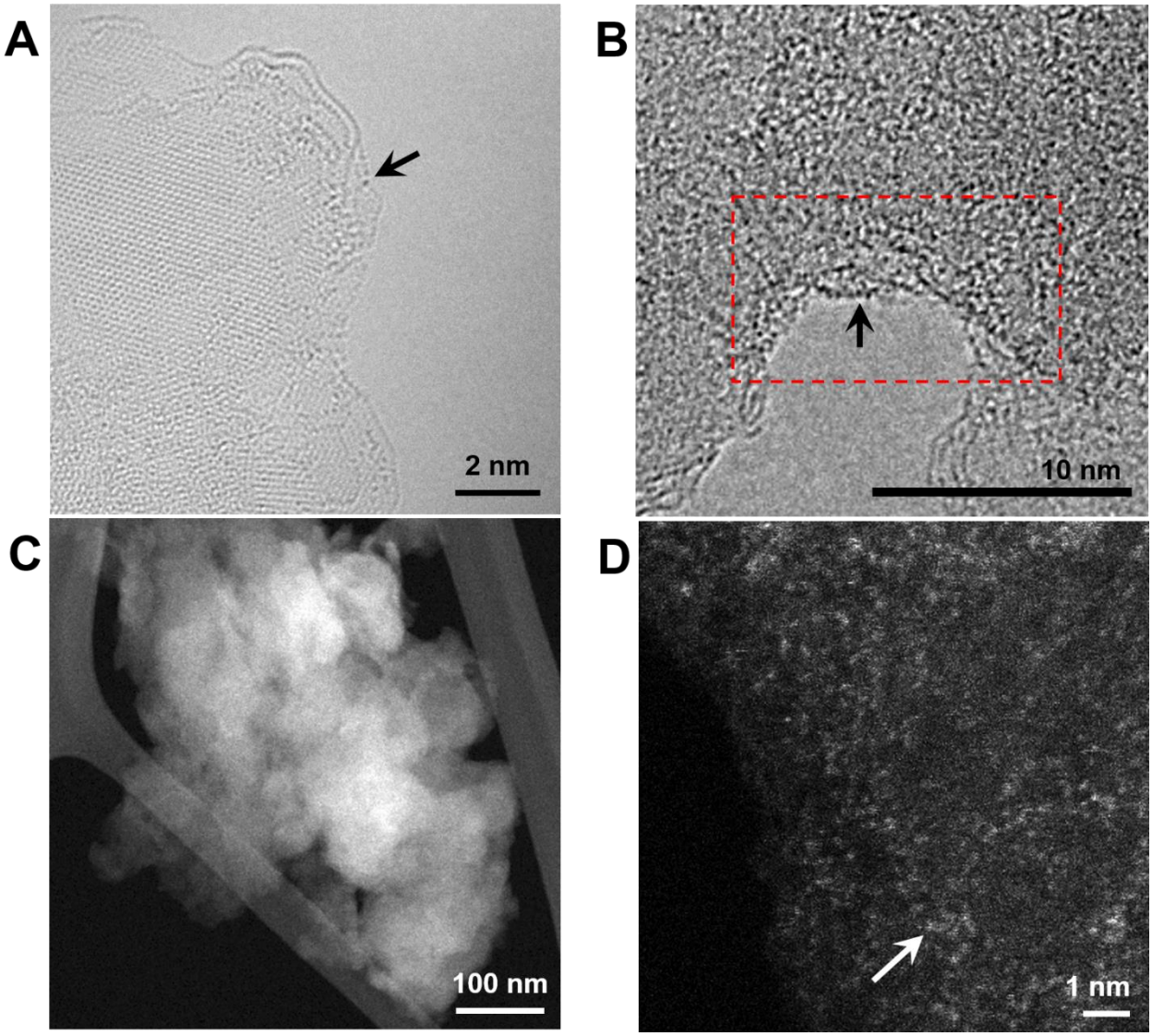

fig. S8. (A) Atomic resolution TEM (AR-TEM) image obtained at the edges of SeGnPs, showing selenium atoms (arrow, black dots) along the edge lines; **(B)** High-resolution TEM (HR-TEM) image focused at the edges of SeGnPs, showing large number of selenium atoms (arrow, black dots) along the edge lines; **(C)** High angle annular dark field (HAADF) STEM of bulk SeGnP powder; **(D)** Magnified HAADF STEM image showing the single Se atoms in bulk solid state.

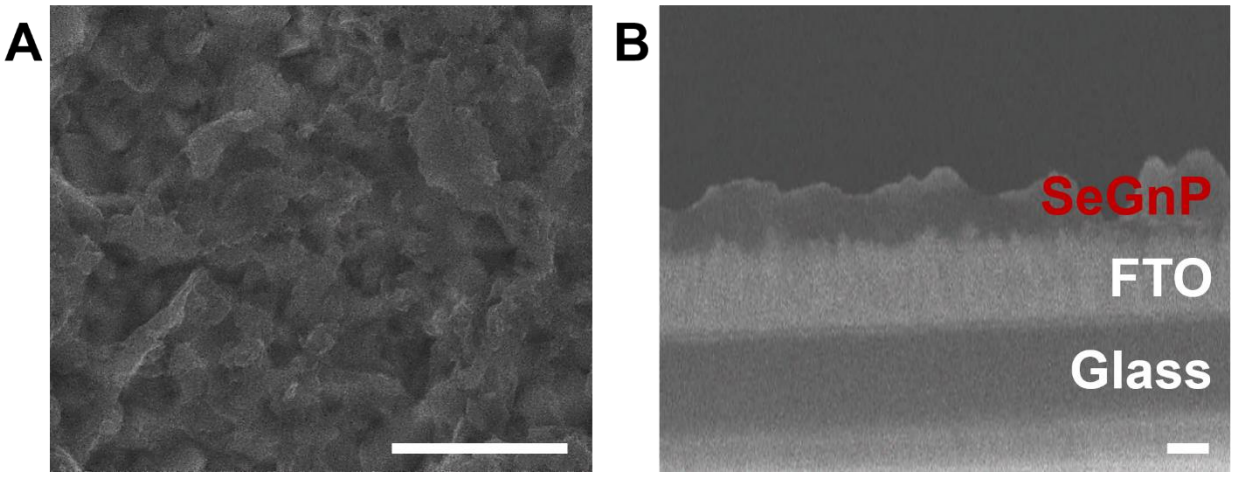

fig. S9. SEM images of SeGnP-coated on FTO: **(A)** Top view; **(B)** Cross sectional view. Scale bars are 1 μm.

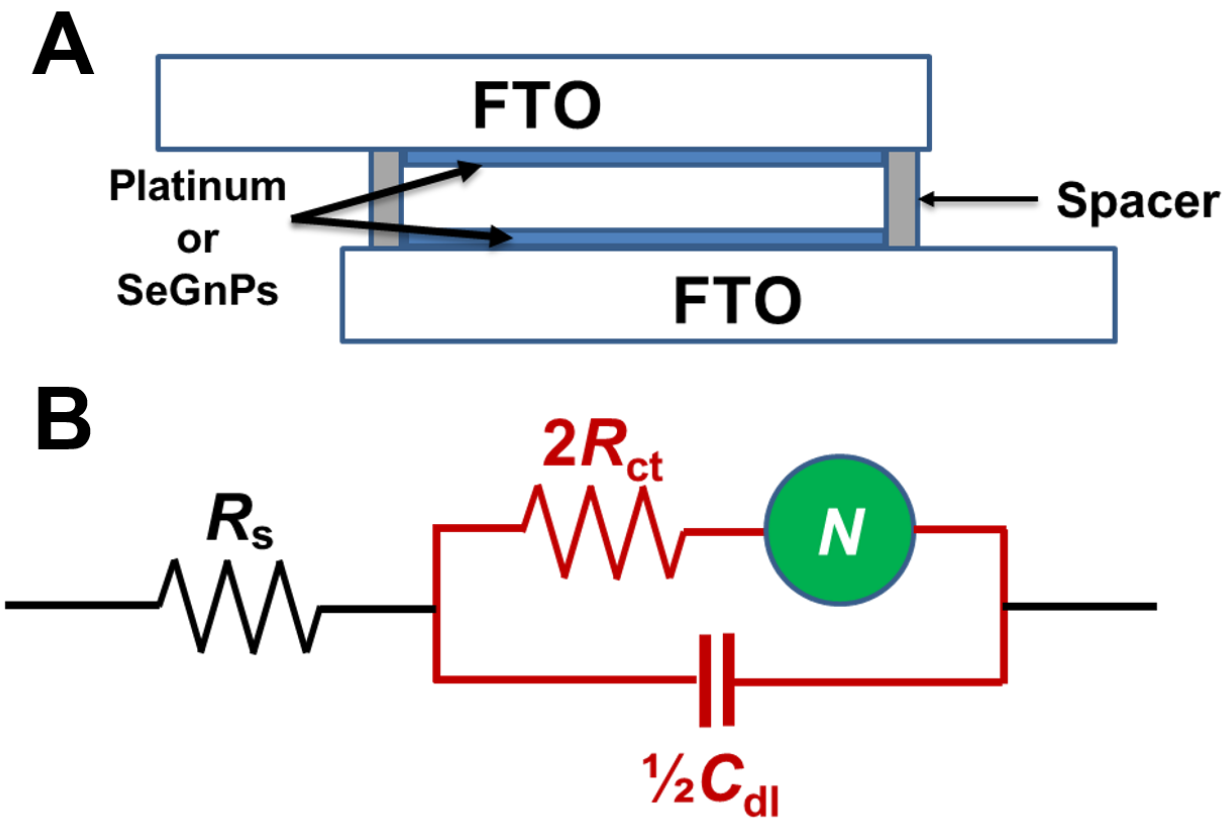

fig. S10. (A) Schematic representation of symmetrical dummy cell with two identical electrodes, **(B)** An equivalent circuit for fitting the impedance spectra having two semicircles characteristic.

Equivalent circuit. In fig. S10B, *N*: Nernst diffusion impedance of the redox couple between two electrodes; R_{ct}: charge-transfer resistance of one electrode at the CE/electrolyte interface, which is directly related to a reaction barrier in the reduction of the redox couple at the CE surface, and hence it should be considered as an important parameter to evaluate the electrocatalytic activities of the CEs in DSSCs. C_{dl}: double layer capacity of one electrode, which is the corresponding capacitance from constant phase element (CPE), stems from the charge accumulation at the CE/electrolyte interface, and depends on the effective surface area of the interface. R_s: serial resistance (TCO electrode).

Electrochemical impedance spectroscopy (EIS), with an appropriate equivalent circuit (EC), is a powerful and useful tool to provide supporting evidence for the CE's performance. In particular, EIS can be used to elucidate the R_{ct} at the CE/electrolyte interface for reduction of the redox species. In general, the electrocatalytic reduction of redox species at the CE indicates the cathodic performance of DSSCs and influences photocurrent generation at the photoanode through dye regeneration. The rate of redox mediator's reduction at the CE should be comparable to the rate of dye regeneration at the photoanode, which is expressed by the photocurrent density (J_{sc}). Hence, to avoid electron loss at the CE, the J_{sc} should be comparable to the exchange current density (J_0) at the CE, which is characterized by a charge-transfer resistance (R_{ct}) (*56*)

$$J_0 = RT/nFR_{ct} \quad (1)$$

where R is the gas constant, T is the temperature, F is the Faraday's constant and n is the number of electrons involved in the electrochemical reduction of redox couple at the CE. Therefore, the J_0 is a kinetic component that arises due to the charge transfer from CE to redox couple at the CE/electrolyte interface.

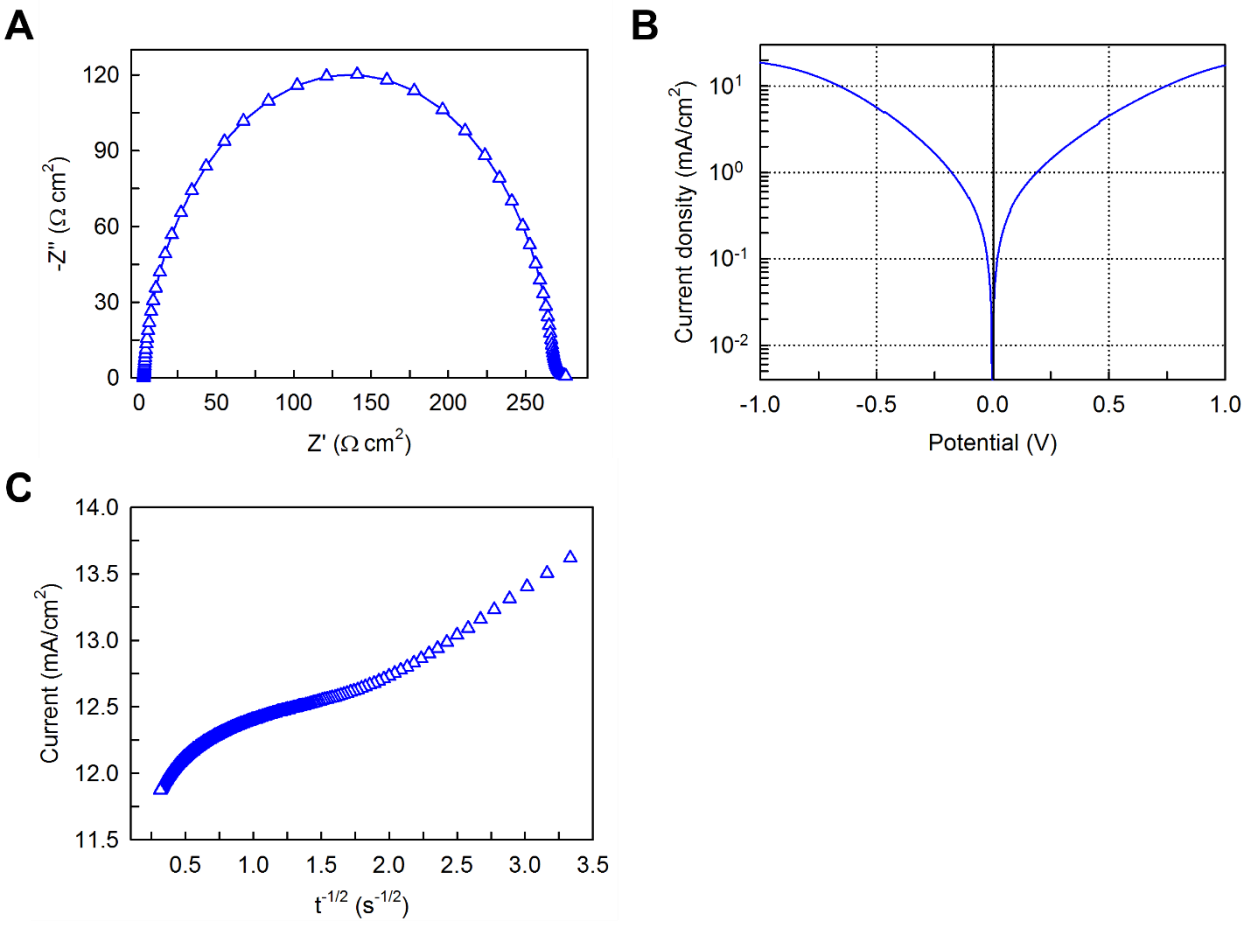

fig. S11. Electrocatalytic activities of the HGnP dummy cell in $Co(bpy)_3^{2+/3+}$ electrolytes at 25°C: **(A)** Nyquist plot; **(B)** Tafel plot; **(C)** CA plot.

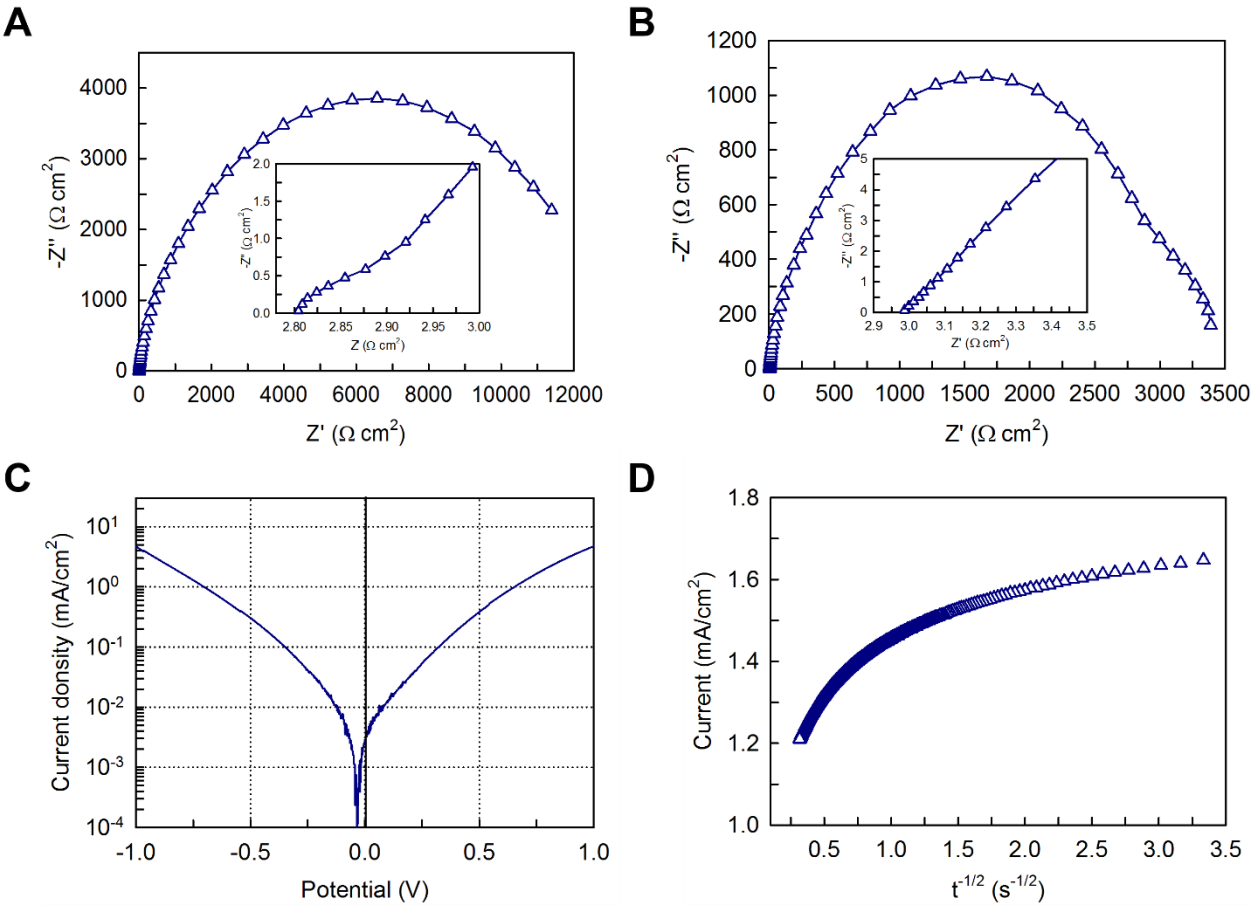

fig. S12. Electrocatalytic activities of the reference HGnP dummy cell in I^-/I_3^- electrolytes. Nyquist plots at difference temperature: **(A)** 25°C; **(B)** 65°C. The insets are enlarged EIS spectra in the high-frequency scan range; **(C)** Tafel plot for I^-/I_3^- electrolytes; **(D)** CA plot for I^-/I_3^- electrolytes.

Electrocatalytic activities of the reference HGnP dummy cell. As can be seen in figs. S11 and S12, HGnPs have poor interfacial charge-transfer activity in both $Co(bpy)_3^{2+/3+}$ and I^-/I_3^- redox couples. The poor interfacial charge-transfer activity is due to the fewer active edges on their crystal lattice.

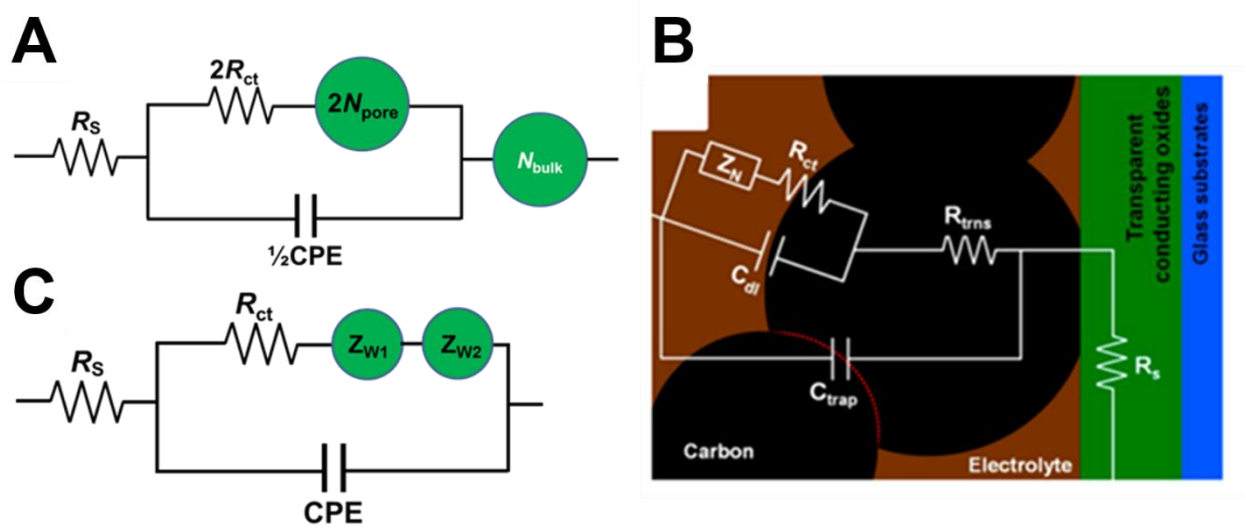

fig. S13. (A) An equivalent circuit (EC) model proposed by Roy-Mayhew *et al.* (*14*); **(B)** An EC model proposed by Rhee *et al.* (*57*); **(C)** Another EC model proposed by Li, G. R and Dou, Y *et al.* (*58*).

Equivalent circuit (EC) models. In the model (fig. S13A), R_s: series resistance; R_{ct}: charge transfer resistance of one electrode at the CE/electrolyte interface; CPE: a constant phase element of one electrode due to electrode roughness instead of an ideal capacitance; N_{pore}: Nernst diffusion impedance of electrolytes within electrode pores; N_{bulk}: Nernst diffusion impedance of electrolytes between the electrodes. In order to identify and quantify the appropriate effects of the N_{pore}, Roy-Mayhew *et al*. proposed that high-, mid-, and low-frequency regions are ascribed to diffusion resistance (N_{pore}) in the pores of electrode, catalytic charge-transfer resistance (R_{ct}) at the CE/electrolyte interface, and ionic diffusion (N_{bulk}) in bulk electrolyte solution, respectively. Thus, the effective charge-transfer resistance ($\mathcal{R}_{ct}$) is introduced (*59*)

$$\mathcal{R}_{ct} = R_{ct} + N_{pore} \quad (2)$$

It is considered that the mass transport of the redox couple in the bulk electrolyte solution is one of the main factors affecting the efficiency of a DSSC, which is also affected within the structural porosity of the electrode. This factor is particularly critical for large redox messengers such as Co-complex-based redox couples, which generally suffer from slow diffusion through nanomaterials with high porosity (*60*). In Fig. 2A, EIS spectra show two distinct semicircles corresponding to charge-transfer resistance (R_{ct}) at high frequency and the Nernst diffusion impedance (Z_N) of the $Co(bpy)_3^{2+/3+}$ redox couple in the electrolyte solution at low frequency regions, respectively. In the present study, N_{pore} at the porous SeGnPs for $Co(bpy)_3^{2+/3+}$ redox couple can be neglected because similar semicircles were observed with the Pt CE surface, where the catalytic reaction occurs on the vertically nonporous Pt surface. Therefore, the R_{ct} itself is the effective charge-transfer resistance ($\mathcal{R}_{ct}$). However, in case of SeGnPs for I^-/I_3^- electrolyte, it is still in doubt that first semicircle is diffusion resistance induced in the pores of the SeGnPs electrode. In addition, it is not logical that any diffusion impedance manifests itself at higher frequency than the parallel pair of R_{ct} and C_{dl} under the no-bias condition.

In the EC model (fig. S13B) proposed by Rhee *et al*. (*57*) to analyze the EIS of porous carbons by considering the electron transport resistance (R_{trns}) and the capacitance of traps (C_{trap}) in the carbon layer itself, the latter was assigned to dangling bonds or surface radicals in the high-frequency semicircle, and the mid- and low-frequency semicircles are due to the catalysis (R_{ct}) and diffusion (Z_N), respectively. Here, it is not clear why any charge-transport resistance (R_{trans}) and capacitance due to trapped electrons in the carbon layer itself (C_{trap}) did not appear for the $Co(bpy)_3^{2+/3+}$ redox couple (Fig. 2A).

In the other EC model (fig. S13C), the mid-frequency semicircle (Z_{w1}) is due to an adsorption of iodine and triiodide on electrode, with the high- and low-frequency semicircles stemming from charge transfer (R_{ct}) and diffusion (Z_{w2}), respectively (*58*). In electrode reaction steps, charge-transfer process at the CE/electrolyte interface occurs in series of steps that ions are adsorbed on electrode surface and then desorption of ions occurs through electron transfer to solvated ions, thus whose kinetics is slower than ions adsorption on the electrode surface. In addition, this assumption is also non-logical that the semicircle (Z_{w1}) is due to an adsorption on electrode at lower frequency than the parallel pair of R_{ct} and C_{dl}. Furthermore, we note that while the traditional Pt EC and EC suggested by Roy-Mayhew *et al.* (*14*) are used with symmetrical cells to back out the resistance of a single electrode (hence the $2R_{ct}$), the other two models are for a single electrode (figs. S13B and S13C).

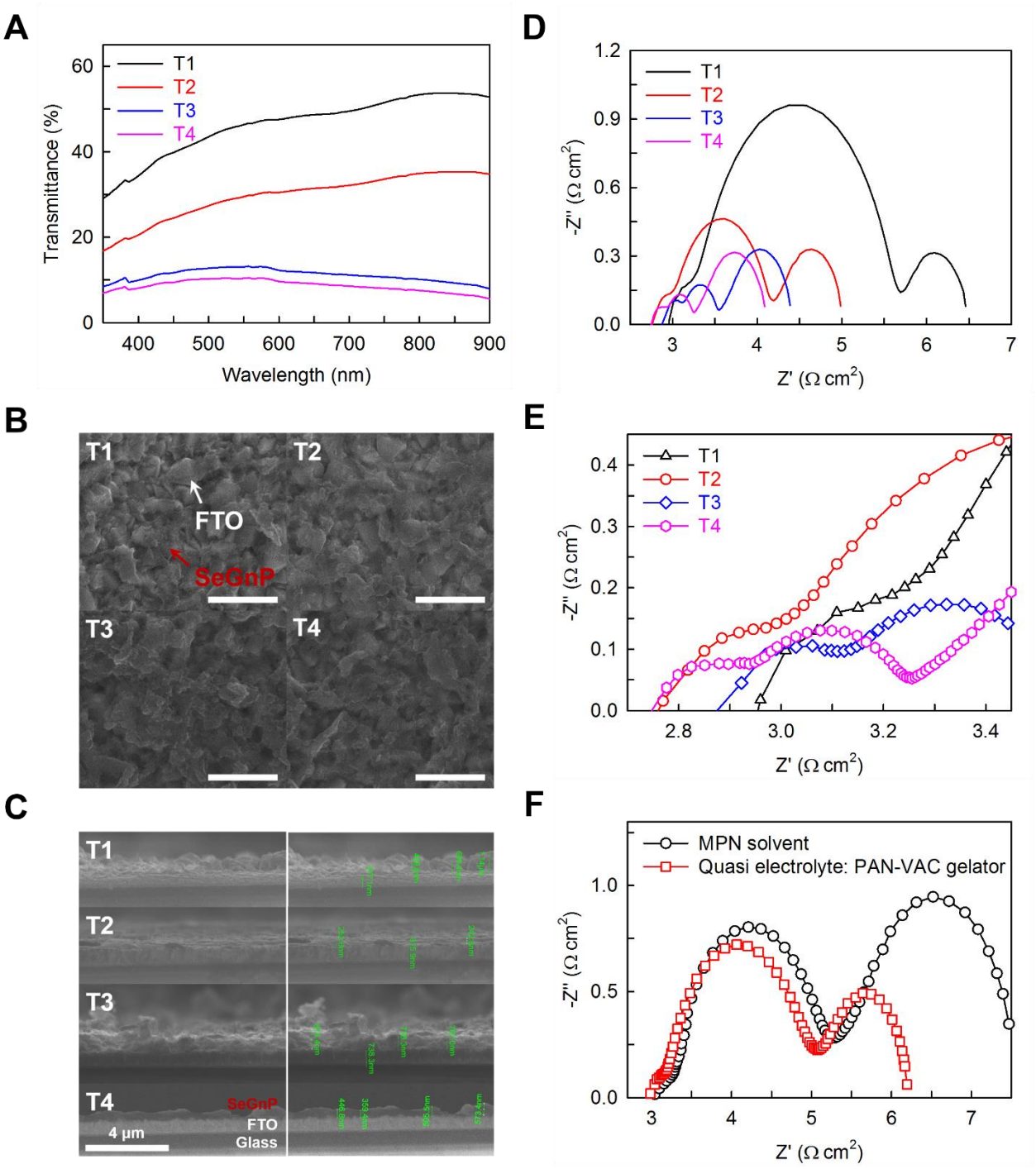

fig. S14. (A) Optical transmittance (T) of SeGnPs on FTO/glass substrates. SEM images: **(B)** Top-view. Scale bars are 1 μm; **(C)** Cross-sectional view with respect to thickness. **(D)** Nyquist plots on I^-/I_3^- redox couple in acetonitrile (ACN) solvent with respect to the thickness of SeGnP-CE; **(E)** Enlarged spectra in frequency range of fig. S14D; **(F)** Nyquist plot on I^-/I_3^- redox couple in 3-methoxypropionitrile (MPN) solvent and quasi-solid electrolytes (*61*).

Dependence of electrode thickness and electrolytes. In fig. S14D, semicircles appeared in high-frequency were slightly decreased with increasing the electrode, but semicircles appeared in mid-frequency region was significantly decreased with increasing the electrode thickness, whereas final circles related with Nernst diffusion in bulk electrolyte solution at low-frequency regions were almost same regardless of thickness. Furthermore, in MPN solvent and quasi-solid electrolytes, first semicircles are almost same with that of ACN solvent, whereas the second circles and Nernst diffusion resistance are higher than those of ACN solvent (fig. S14F).

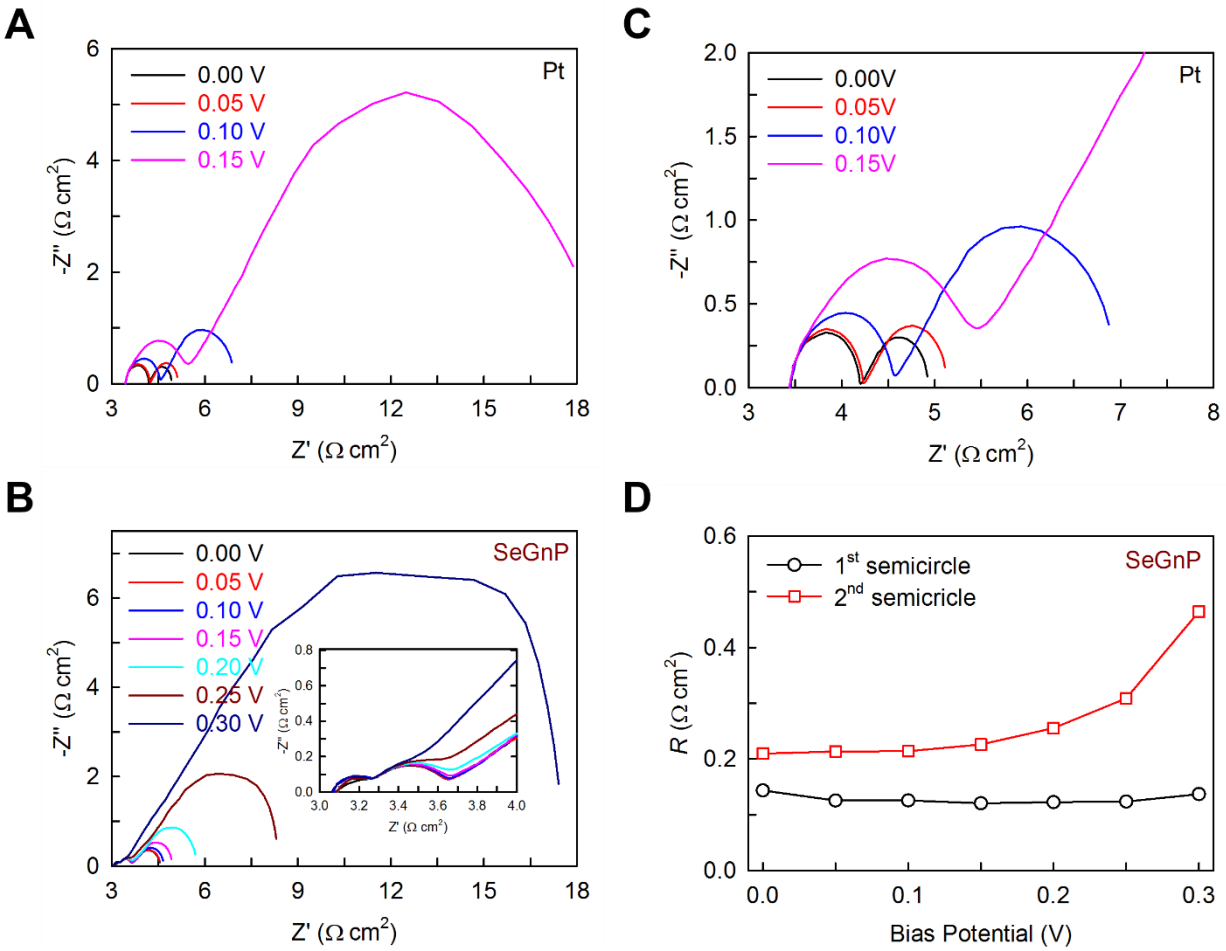

fig. S15. Nyquist plots obtained from the symmetrical dummy cells with Pt and SeGnP electrodes as a function of applied bias potential on I^-/I_3^- redox couple in acetonitrile: **(A)** and **(B)** Full-frequency range, and the inset of fig. S15B is high-frequency regions; **(C)** High-frequency regions of Pt; **(D)** Resistance changes in SeGnPs as a function of external applied potential.

Dependence of applied bias potential. Actually, the R_{ct} is defined originally in equilibrium. However, if a bias potential is applied to the cell, ion concentrations are different at the anode and the cathode, thus their R_{ct} are different, in this case, the R_{ct} must be interpreted as a differential resistance, *i.e.* $R_{ct} = \partial V/\partial I$ (*62*). First semicircle of Pt, second semicircle of SeGnPs and their Nernst diffusion (Z_N) were increased with increasing the applied external potential, whereas first semicircles of SeGnPs electrode were not significantly influenced by the external applied potential

(fig. S15D). The R_{ct} values of the Pt and SeGnPs increases with increasing the bias potential to the cells, this increase can be explained qualitatively by faster electrode kinetics for applied bias potentials, as expressed by the Butler-Volmer equation (*62*)

$$i = i_0 \left(\frac{C_O(0,t)}{C_O^*} e^{-\alpha f \eta} - \frac{C_R(0,t)}{C_R^*} e^{(1-\alpha) f \eta} \right) \quad (3)$$

where i_0 is exchange current density, α is charge transfer coefficient, f is F/RT, and η is E-E_{eq}, overpotential. Note that the first term describes the cathodic component current at any potential, and the second gives the anodic contribution. With increasing the bias potentials, the concentration of I_3^- at the cathode surface is depleted and is given by (*21*)

$$c^0_{I_3^-} = c_{I_3^-} \left(1 - \frac{I_{DC}}{I_{lim}} \right) \quad (4)$$

where C_{I3^-} is the concentration of I_3^- in equilibrium, I_{DC} is DC current, and I_{lim} is the diffusion-limited current. I_3^- is produced at the anode. The changes in concentration of I^- can be neglected because of the large excess of I^- in the electrolyte. The increased R_{ct} is due to the depletion of I_3^- at the cathode surface or pores. Furthermore, it is obvious that the described depletion of electroactive species from the cathode vicinity increases also the Nernst diffusion impedance (Z_N) in the bulk electrolyte solution.

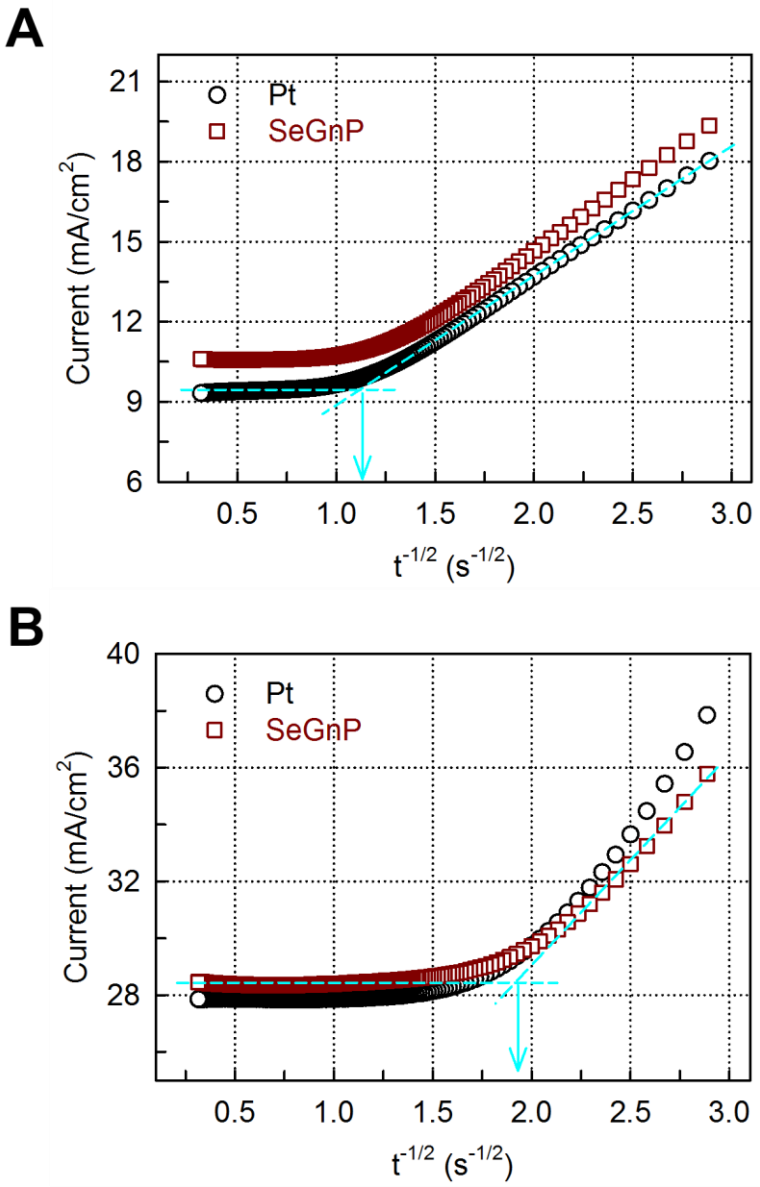

fig. S16. Potential step CA curves on symmetrical dummy cells with the Pt and SeGnPs electrodes. Potential was from 0 to 0.7 V for 10 s: **(A)** $Co(bpy)_3^{2+/3+}$; **(B)** I^-/I_3^-.

Potential-step chronoamperometry. To examine the mass transport properties, CA measurements were carried out at room temperature. Shortly after the potential step, the current follows the semi-infinite Cottrell-like decay (J_{Cott}). The current drops linearly with $t^{-1/2}$ (t is time) as long as the concentration profiles in front of each electrode merge to form a single linear profile.

At this stage, the current attains a steady state value, which is equal to the limiting current (J_{lim}). Extrapolation of both linear components of the CA plots, i.e., from a condition of $J_{Cott} = J_{lim}$, provides intersection at the so-called transition time (t), which provides the diffusion coefficient D according to the Eq. (6)

$$\frac{nFAC \cdot \sqrt{D}}{\sqrt{\pi t}} = \frac{2nFAC \cdot D}{\delta} \tag{5}$$

$$D = t^{-1}\left(\frac{\delta^2}{4\pi}\right) \tag{6}$$

As can be seen, Pt and SeGnPs reached to the steady-state current instantly after the potential stepping in both $Co(bpy)_3^{2+/3+}$ and I^-/I_3^- electrolytes.

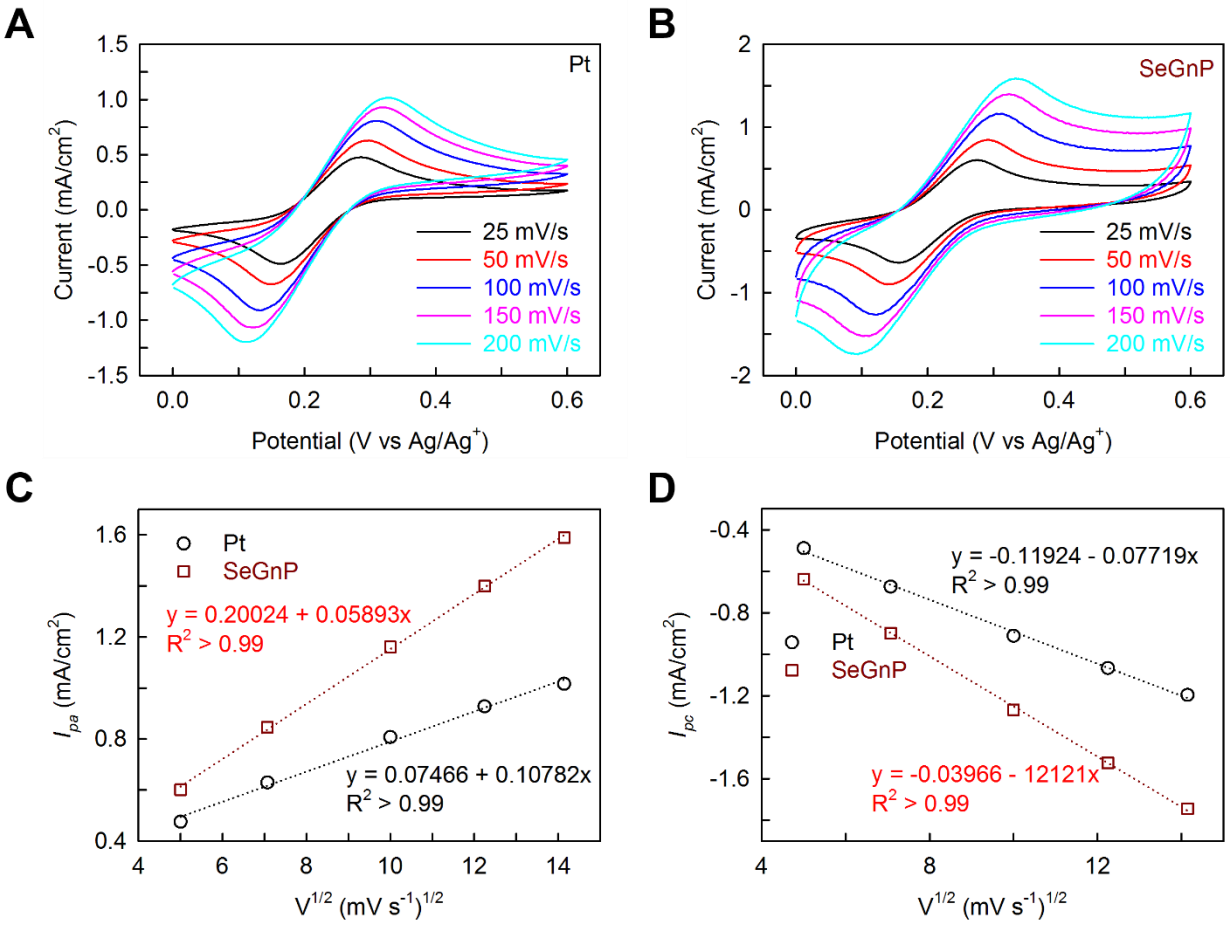

fig. S17. Cyclic voltammograms as a function of scan rate in $Co(bpy)_3^{2+/3+}$ redox couple: **(A)** Pt; **(B)** SeGnP electrodes as the working electrodes, a Pt wire as the CE, Ag/Ag^+ as the reference electrode and 0.1 M $LiClO_4$ as the supporting electrolyte; **(C)** Oxidation and **(D)** Reduction peak currents with respect to the square root of scanning rate.

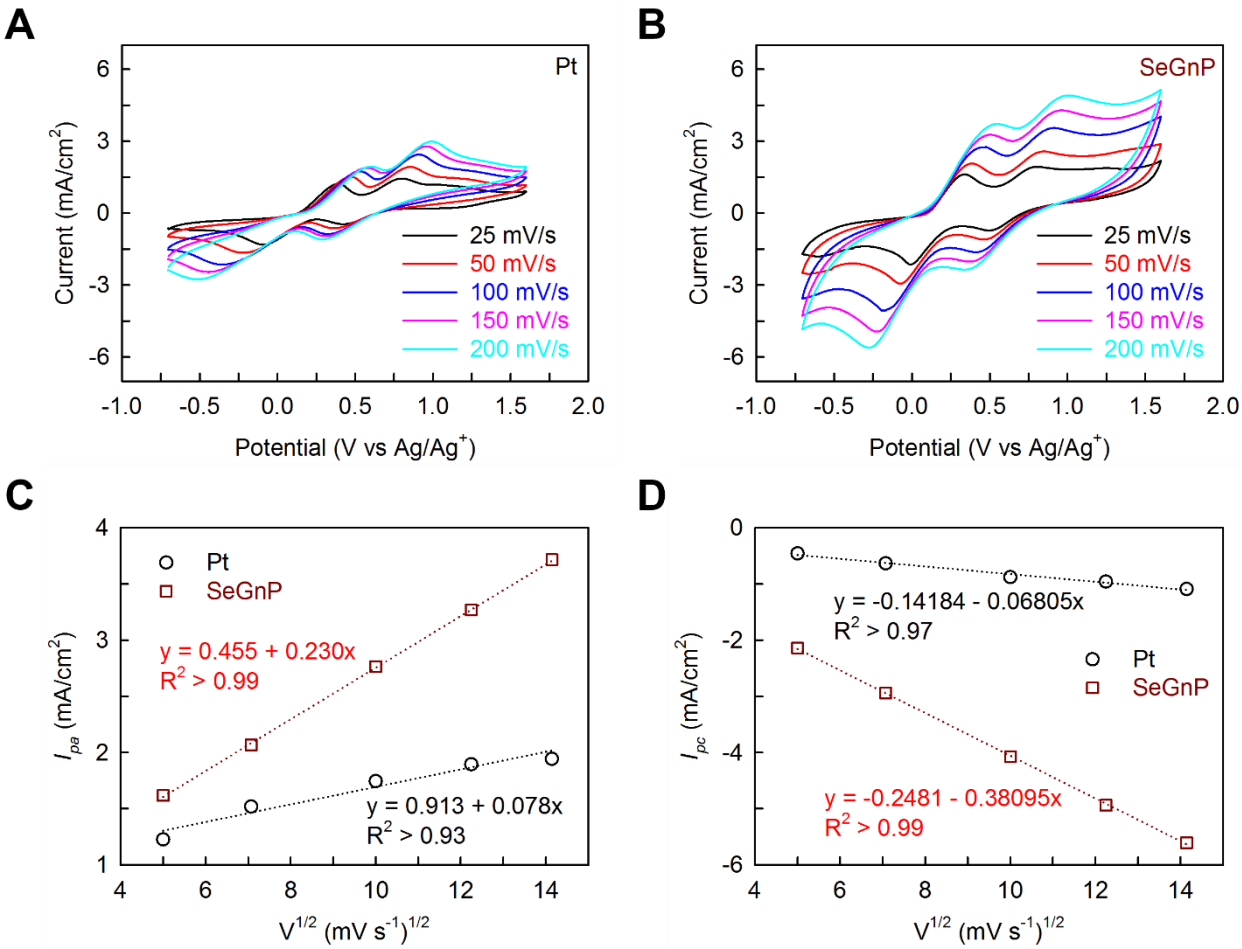

fig. S18. Cyclic voltammograms as a function of scan rate in I^-/I_3^- redox couple: **(A)** Pt; **(B)** SeGnP electrodes as the working electrodes, a Pt wire as the CE, Ag/Ag^+ as the reference electrode and 0.1 M $LiClO_4$ as the supporting electrolyte; **(C)** Oxidation and **(D)** Reduction peak currents with respect to the square root of scanning rate.

Dependence of scan rate. The linear relationship between redox peak currents and scan rates indicates that SeGnPs possess high electrocatalytic activity towards the redox of $Co(bpy)_3^{2+3+}$ (figs. S17C and S17D) and I^-/I_3^- (figs. S18C and S18D) and the redox reactions on SeGnPs are controlled by both the R_{ct} at the electrode/electrolyte interface and ionic diffusion in the bulk electrolyte, which are well agreed with the EIS (Figs. 2A and 2B) and CA (fig. S16) measurements.

That is, the SeGnP electrode is favorable for fast electron transfer, which is also helpful to improve the electrocatalytic activity for the $Co(bpy)_3^{2+/3+}$ and I^-/I_3^- redox couples.

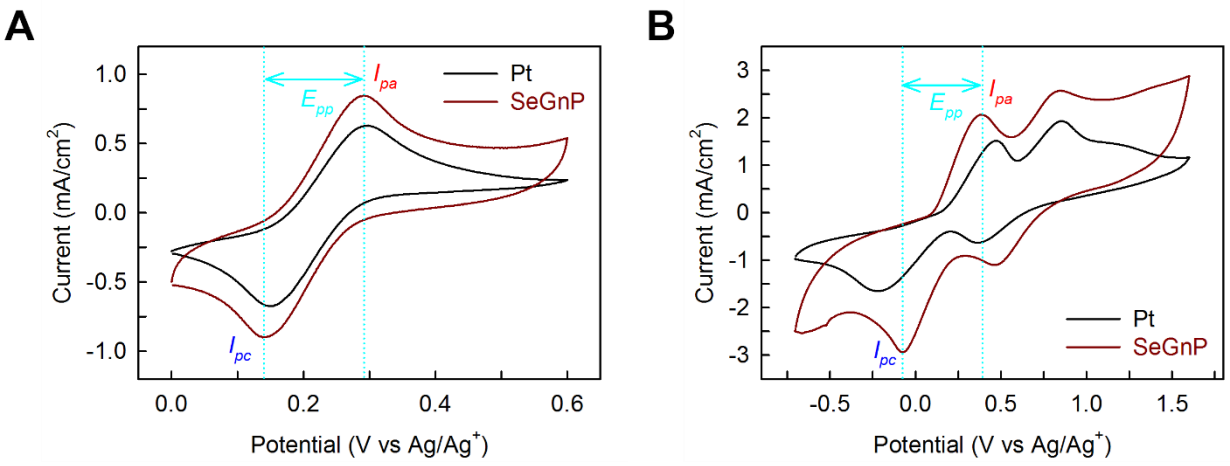

fig. S19. Cyclic voltammograms obtained at a scan rate of 50 mV s^{-1} using Pt and SeGnP electrodes as the working electrodes, a Pt wire as the CE, Ag/Ag^+ as the reference electrode, and 0.1 M $LiClO_4$ as the supporting electrolyte: **(A)** $Co(bpy)_3^{2+/3+}$; **(B)** I^-/I_3^- redox couples.

Comparison between SeGnPs and Pt. An anodic peak current (I_{pa}) and a cathodic peak current (I_{pc}) were observed, which corresponded to the oxidation of $Co(bpy)_3^{2+}$ and I^- ions and the reduction of $Co(bpy)_3^{3+}$ and I_3^- ions, respectively. Moreover, the peak to-peak separation (E_{pp}) is 0.149 and 0.148 V in Pt and SeGnP electrodes for $Co(bpy)_3^{2+/3+}$ redox couple, respectively. For I^-/I_3^- redox couple, the E_{pp} is 0.298 and 0.256 for the Pt and SeGnP electrodes, respectively. As compared to Pt, SeGnPs exhibits narrower E_{pp} and higher I_{pa} and I_{pc}, indicating that the reduction rate on the SeGnP surface is faster than that on the Pt counterpart, which was also confirmed in the CV measurements with different scan rates (fig. S18). The high peak current densities and low E_{pp} are responsible for the excellent electrocatalytic activity.

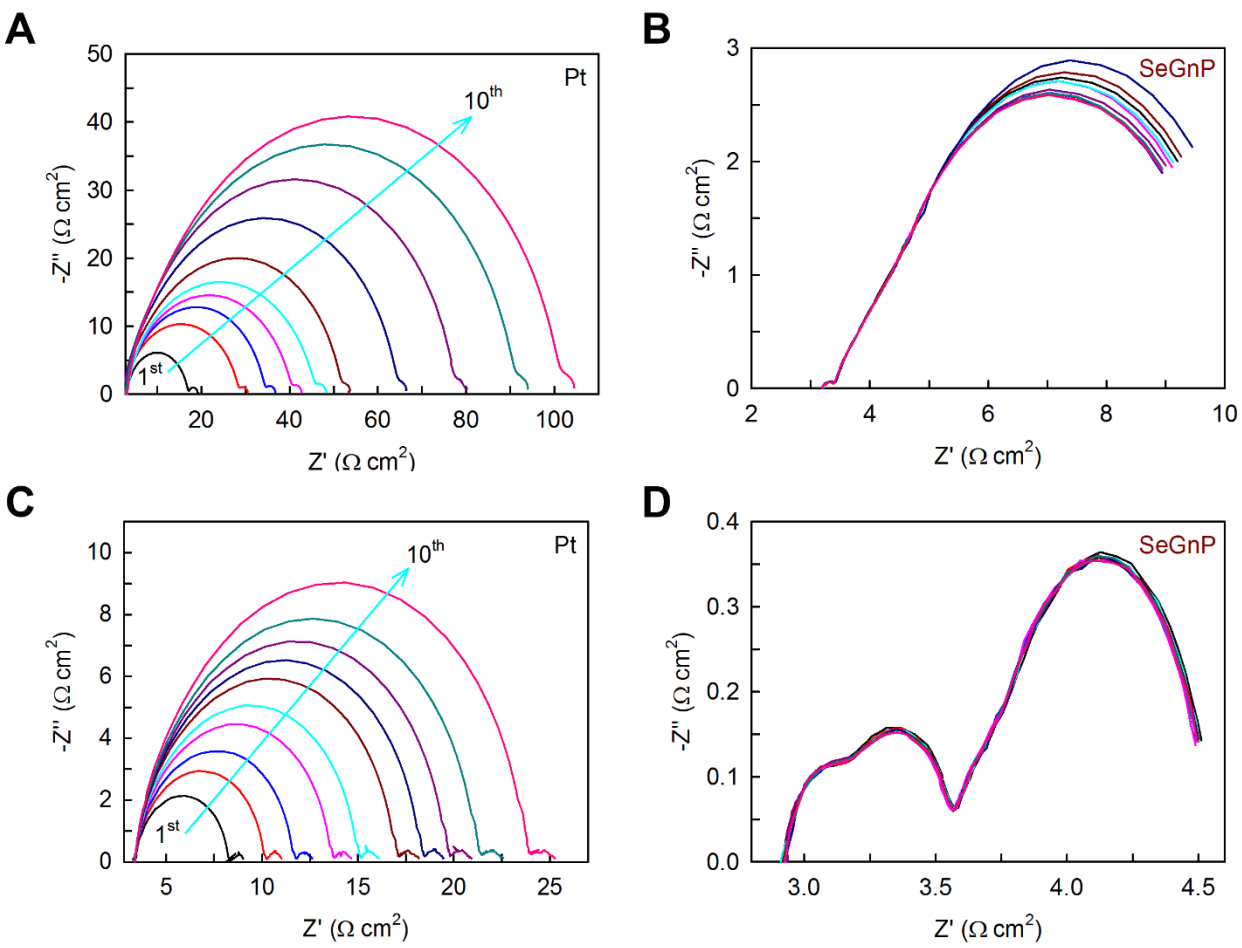

fig. S20. Nyquist plots of the symmetrical dummy cells with different CEs on $Co(bpy)_3^{2+/3+}$ and I^-/I_3^- electrolytes. The sequence of measurements is as follows: 100 × CV scans (from 0 V → 1 V→ –1 V→ 0 V at a scan rate of 50 mV s^{-1}) followed by 60 s relaxation at 0 V and then EIS measurement at zero bias potential. The sequence of electrochemical test was repeated 10 times: **(A)** Pt; **(B)** SeGnPs in $Co(bpy)_3^{2+/3+}$ electrolytes, respectively; **(C)** Pt; **(D)** SeGnPs in I^-/I_3^- electrolytes, respectively.

Electrochemical stability. As-prepared dummy cells were subjected to a repeated treatment to evaluate the electrochemical stability of the CEs through CV at room temperature followed by EIS measurements. Despite cycling potentials, the semicircles in the low-frequency region exhibited a similar shape between the sample electrodes. These similar curves indicate that the $Co(bpy)_3^{2+/3+}$

and I^-/I_3^- redox couples were invariant with the surface conditions at the electrodes. However, the R_{ct} of the Pt electrode significantly increased compared to those of the SeGnP-CE as the cycling potential was repeated (figs. S20A and S20C). The R_{ct} values of Pt and SeGnPs were 6.97 (fig. S20A) and 0.13 Ω cm^2 (fig. S20B) in the first cycle, *e.g.*, after 100 CV cycles, for the $Co(bpy)_3^{2+/3+}$, respectively. For the I^-/I_3^- redox couples in the first cycle, they were 2.43 (fig. S20C) and 0.42 Ω cm^2 (fig. S20D), respectively. In the final cycle, *e.g.*, after 1,000 CV cycles, the R_{ct} values of Pt and SeGnPs were 49.61 (fig. S20A) and 0.13 Ω cm^2 (fig. S20B) for the $Co(bpy)_3^{2+/3+}$ redox couple, 10.25 (fig. S20C) and 0.44 Ω cm^2 (fig. S20D) for the I^-/I_3^- redox couple, respectively. Furthermore, one-month later after CV 1,000 cycles for the $Co(bpy)_3^{2+/3+}$, the R_{ct} of SeGnPs was 0.17 Ω cm^2 (fig. S21). The R_{ct} of SeGnPs for the I^-/I_3^- redox couple was 0.43 Ω cm^2 (R_{tm} of 0.24 and R_{ct} of 0.29 Ω cm^2 (fig. S21), respectively, demonstrating that excellent electrochemical stability for SeGnPs can be delivered in both electrolytes.

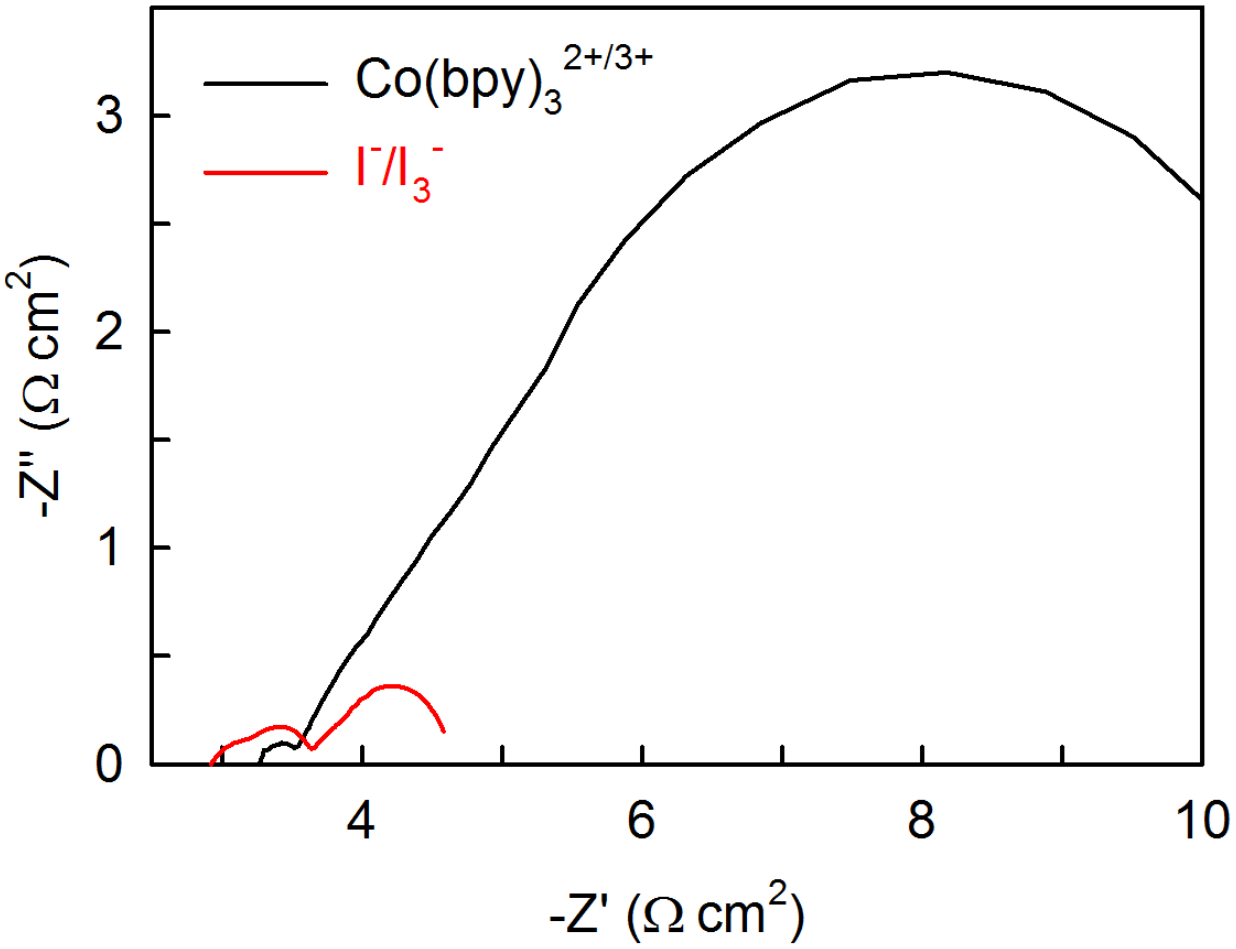

fig. S21. Nyquist plots measured at one-month later after 1,000 cycling measurements with the SeGnP dummy cells for $Co(bpy)_3^{2+/3+}$ and I^-/I_3^- redox couples.

II. Computational Section

1. Adsorption of atomic I on pristine and Se-doped graphene edges

Models. All the considered Se-doped GnP models are shown in fig. S22. As the reference systems, we employed hydrogen-passivated graphene nanoribbon (GNR) models with armchair (ac) and zigzag (zz). Armchair and zigzag GNRs were modeled by 8 dimer lines and 5 zigzag chains, respectively (fig. S22A). Preparing edge-doped counterparts, we first considered the doping possibilities where one H atom is replaced by a single-coordinated (c1) Se atom (fig. S22A). For both ac-Se(c1)-GnP and zz-Se(c2)-GnP cases, we have considered the possibility of passivating the Se atom by a H atom to prepare ac-SeH-GnP and zz-SeH-GnP models (fig. S22D). Additionally, we have prepared several ac- and zz-GnP models including a double-coordinated (c2) Se atom in three conformations (fig. S22C). To accommodate the iodine and acetonitrile molecules in various bonding configurations, a vacuum space with the dimension of 1.6 nm and 2.8 nm to its nearest-neighbor periodic images along the GNR out-of-plane and in-plane directions was included. Thus, the supercell size was 17.04×28.00×16.00 $Å^3$ and 14.76×28.00×16.00 $Å^3$ for the acGNR and zzGNR models, respectively.

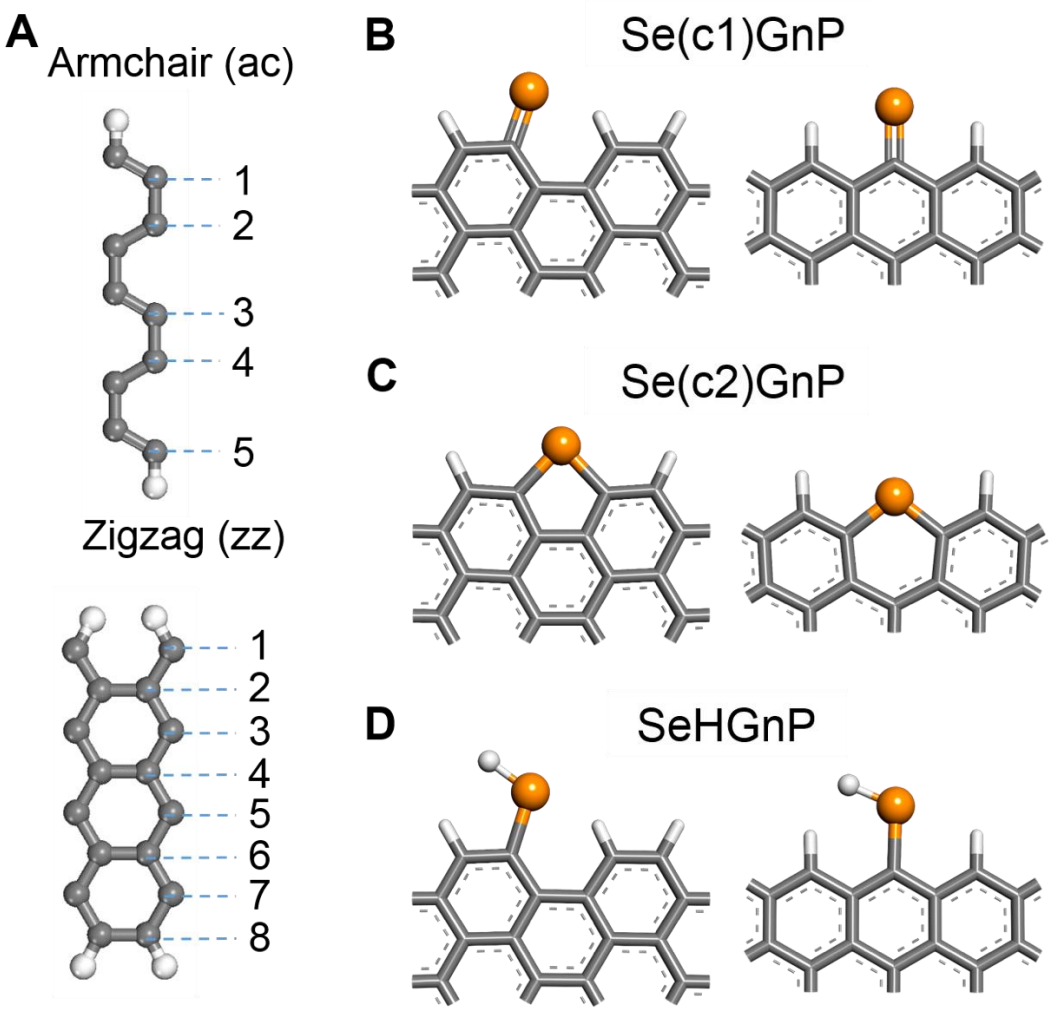

fig. S22. Se-doped graphene models. (A) Unit cell atomic structures of the reference hydrogenated armchair (top) and zigzag (bottom) GNRs that model HGnPs. Starting from the reference structures, we have prepared; **(B)** Two single-coordinated **(**c1) and **(C)** Three double-coordinated (c2) Se atom edge-doped models; **(D)** For the Se(c1)-GnP models, we have also considered the possibility of hydrogen passivating selenium atom.

Methods. The atomic geometries were optimized by carrying out density functional theory (DFT) calculations with the VASP code (*28*). We performed all the calculations allowing spin polarization within the Perdew-Burke-Ernzerhof parametrization of generalized gradient approximation (*29*) corrected by the DFT-D3 method for dispersion interactions (*30*). The ideal hydrogenated zigzag graphene edges are known to be ferromagnetically aligned, while for GNRs the two edge states are antiferromagnetically ordered (*27, 63*). This magnetic edge states were also predicted to be preserved in various defected and doped edge cases (64–*67*). We thus assigned such initial spin configurations in treating the zigzag GNR models. Valence electronic states were expanded in plane wave basis sets with the 400 eV energy cut off, and the project-augmented wave method was used to represent core-valence electron interactions (*31*). In the geometry optimization processes, ionic degrees of freedom were relaxed using the BFGS minimization scheme until the Hellman-Feynman forces on each ion were less than 0.01 eV/Å. The single Γ-point was sampled after confirming that a higher-resolution 2×1×2 k-point mesh applied to a pre-checking test model results in negligible changes in bond length and binding energy.

Adsorption geometries and energies of the I atom to GnP. To evaluate the catalytic activities of the selenium atom in various doping configurations shown in fig. S23, we calculated the I atom adsorption energies according to (*22, 25*)

$$E_{ads} = E_{GnP} + \frac{1}{2}E_{I_2} - E_{I-GnP} \quad (7)$$

where E_{GnP}, E_{I_2}, and E_{I-GnP} are the total energies of the GNR, I_2 in the gas phase, and GnP adsorbed by an I atom, respectively. Each energy term was obtained from independent fully-optimized geometries. Among various models, both armchair and zigzag Se(c1)-GnP models were found to meet the iodine atom adsorption criterion for the good IRR activity (Fig. 3A). The zigzag SeH-GnP model was also identified as a possible candidate.

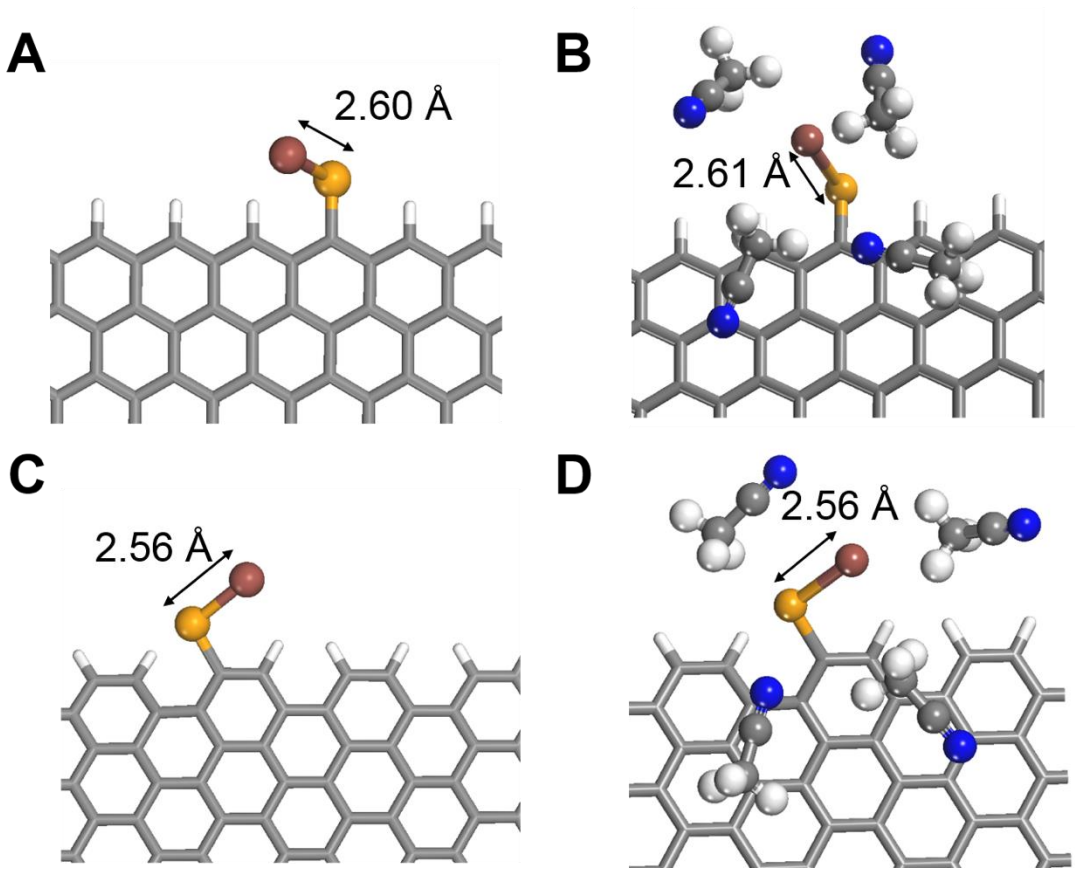

fig. S23. Adsorption geometries of the I atom on Se(c1)-GnP in vacuum and acetonitrile environment. Geometries of the I atom adsorbed ac-Se(c1)-GnP: **(A)** in vacuum; **(B)** solvated by four CH_3CN molecules, and the I atom adsorbed zz-Se(c1)-GnP; **(C)** in vacuum; **(D)** solvated by four CH_3CN molecules. In (**B**) and (**D**), the two acetonitrile molecules on the graphene plane assumed lying-down configurations at the distance of 3.2 Å ~ 3.5 Å from the GnP surface. The variation of bonding distances between selenium and iodine atoms upon the introduction of solvent molecules was negligible.

Solvent effects. To include the solvation effects, we explicitly surrounded the Se-I bonds at the GNR edges by acetonitrile (CH_3CN) molecules. The solvated geometries for the representative Se(c1)-GNP cases are shown in figs. S23B and S23D. It was determined that the thermodynamically most favorable situation is when I^* is surrounded by four CH_3CN molecules, two of which are adsorbed on the GNR plane and the other two are located in the nearby vacuum region. The bond distance between Se and I atoms was found to be negligibly affected by solvent molecules, implying the weak binding nature between the Se-I complex and surrounding acetonitrile molecules.

For the Se(c1)-GnP models that showed the prominent IRR catalytic activities, we tested up to four explicit acetonitrile solvation cases and found that two CH_3CN molecules placed on the GNR sides already provide almost converged results (fig. S24). As we thus report in Fig. 3A, the I adsorption values obtained with two explicit solvent molecules. We comment that this situation is different from the Pt surface cases, where the thermodynamically favorable condition is when three CH_3CN molecules surround I^* and the solvent effects keep increasing with the number of CH_3CN molecules (*25*).

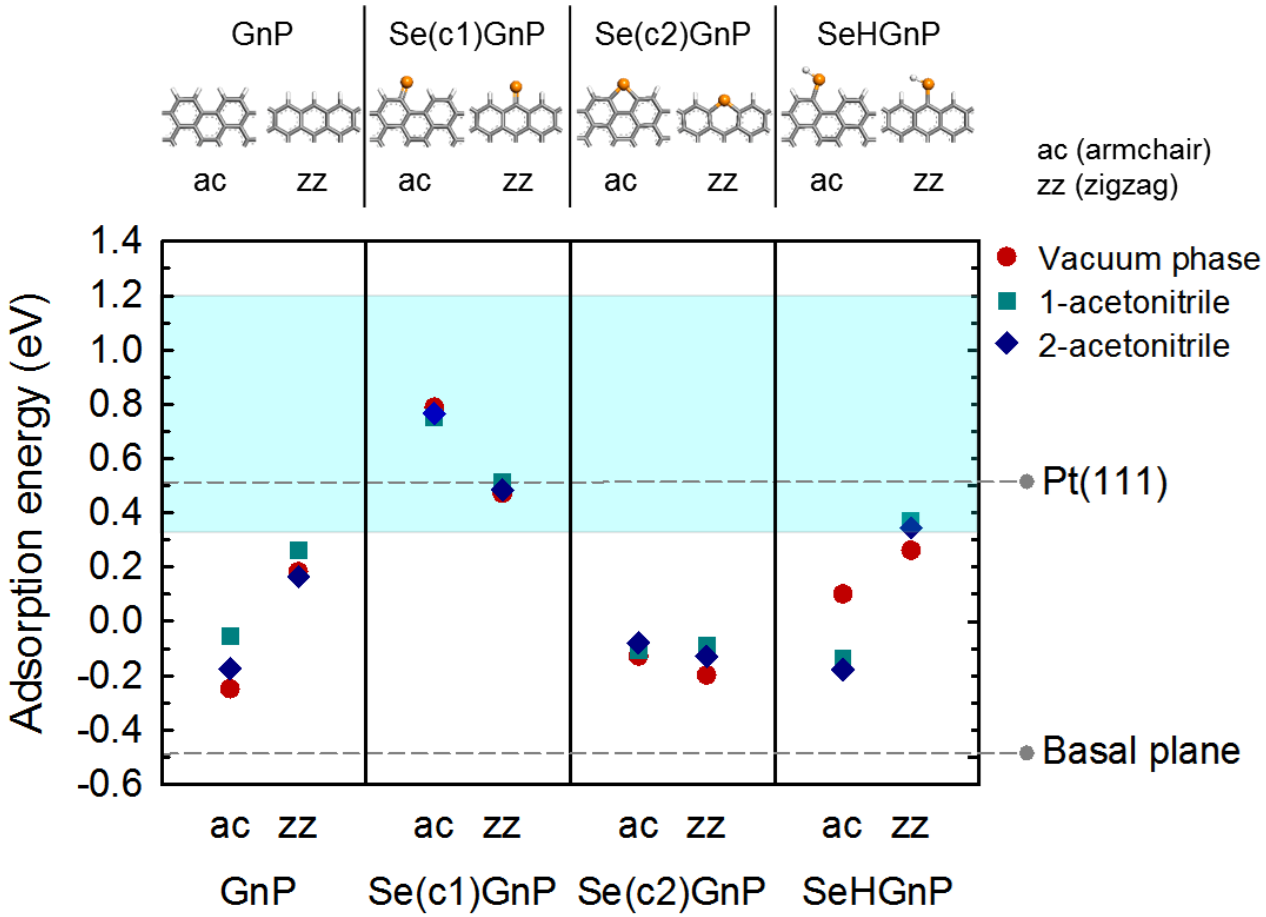

fig. S24. For various Se-doped armchair (ac) and zigzag (zz) graphene edge models (top panel), the adsorption energies of the I atom with up to two explicit acetonitrile solvent molecules have been evaluated (bottom panel). In the bottom panel, the cyan shaded region indicates where the IRR activity criterion is satisfied. As the reference points, the I adsorption energies of 0.52 eV for Pt (111) (surrounded by three CH_3CN molecules) (*22, 25*) and –0.49 eV for the graphene basal plane (surrounded by four CH_3CN molecules) are denoted as dash-dot lines.

2. Origin of the first semicircle in the EIS spectra of carbon-based CEs with the I^-/I_3^- redox couple

Computational methods. To investigate the origin of the additional first semicircle in the EIS spectra of carbon-based CE with I^-/I_3^- redox couple, we performed DFT-based non-equilibrium Green's function (NEGF) calculations (*35*, *36*) for the models of infinite graphene adsorbed by I^- and I_3^-. DFT calculations were carried out using the SIESTA software (*32*) within the Perdew-Burke-Ernzerhof parameterization of generalized gradient approximation (*29*). The graphene basal plane was modeled by a supercell composed of 10×10 graphene hexagonal unit cells which consists of 200 carbon atoms (fig. S25A), and a 30 Å of vacuum space was adopted along the plane-normal direction to avoid artificial interactions with periodic images. To obtain the geometries of I_3^- and I^- adsorbed on graphene and their adsorption energies, we applied the Grimme D2 dispersion correction method (*33*). Core electrons were replaced by Troullier-Martins-type norm-conserving pseudopotentials (*34*), and the Kohn-Sham wavefunctions were expended in terms of double-ζ-plus-polarization-level numerical atomic basis sets defined by the confinement energy of 100 meV. Real-space mesh defined with the cut-off energy of 200 Ry was employed for the grid operations, and a 2×2×1 $\vec{k}$-points in the Monkhorst-Pack scheme were sampled. In carrying out calculations for the charged systems (I^-/I_3^--adsorbed graphene), we followed the charge correction procedure proposed by Makov and Payne (*68*) as implemented in SIESTA, which introduces a uniform background charge to make the total charge zero.

In order to compute the electron transport properties of graphene adsorbed by I^- or I_3^-, we next carried out NEGF calculations using the TranSIESTA code (*35*). We chose the charge transport direction along the armchair dimer lines, and starting from an orthogonal graphene cell composed of four C atoms constructed a 5×12 supercell (5 dimer lines and 24 zigzag chains along the transport-normal and transport directions, respectively) as shown in fig. S25A. The supercell was then divided into three equal-area regions, each of which was assigned as the electrode 1,

scattering region, and electrode 2, respectively. This equal division ensures a consistent description of graphene doping induced by I^- or I_3^- (equal doping concentrations in the scattering and electrode regions). Based on the DFT-optimized geometries, a I^- or I_3^- adsorbent was then placed at the center of the supercell (scattering region) and two additional I^- or I_3^- were equidistantly placed along the transport direction (electrode 1 and 2 regions). A fine 20×1×1 Monkhorst-Pack grid was used for the $\vec{k}_\perp$ point sampling along the transport-normal direction. Note that, due to the difference in the supercell geometries, the number density of I^- or I_3^- n_{I^-/I_3^-} (0.47 / nm^2) has been increased from that in the DFT calculation models (0.19 / nm^2).

Transmission functions were calculated according to

$$T(E) = Tr[\Gamma_1(E)G(E)\Gamma_2(E)G^+(E)] \tag{8}$$

where $G(E) = (ES - H + \Sigma_1 + \Sigma_2)^{-1}$ is the retarded Green's function and $\Gamma_{1,2} = i(\Sigma_{1,2} - \Sigma_{1,2}^+)$ is the broadening function. *S* and *H* are respectively the overlap and Hamiltonian matrices of scattering region. The self-energies $\Sigma_{1,2} = x_{1,2} g_{s1,2} x_{1,2}$, where $x_{1,2}$ are the parts of molecule-electrode 1 or 2 contact among the total $ES - H$ matrices and $g_{s1,2}$ are the surface Green's functions, provide the *ab-initio* broadening and shift of energy levels in scattering region caused by the coupling with the electrode regions 1 and 2. The surface Green's functions $g_{s1,2}$, which are essential to correctly describe self-energy, were obtained from two distinct DFT calculations for the electrodes 1 and 2. Along the electron transport direction (indicated as z-direction in fig. S25B), 15 $\vec{k}_\parallel$ points along the transport direction were sampled to generate $g_{s1,2}$. In obtaining *T* (*E*), energy grid from 2.0 eV below to 2.0 eV above the Fermi level E_F was sampled at the 0.01 eV resolution.

Using the $T(E)$, the current-voltage (I-V) characteristics were computed according to the Laundauer- Büttiker formula

$$I(V) = \frac{2e}{h}\int_{\mu_1}^{\mu_2} dET(E,V)[f(E-\mu_1) - f(E-\mu_2)], \tag{9}$$

where μ_1 and μ_2 are the chemical potentials of the electrode 1 and electrode 2, respectively, and f is the Fermi-Dirac distribution function. Here, we obtained low-bias regime I-V curve using the approximation $T(E,V) \approx T(E,0)$. A spatially symmetric distribution of the bias voltage across the electrode 1 - scattering region – electrode 2, or $\mu_1 = E_F - 0.5\ eV$ and $\mu_2 = E_F + 0.5\ eV$, was assumed.

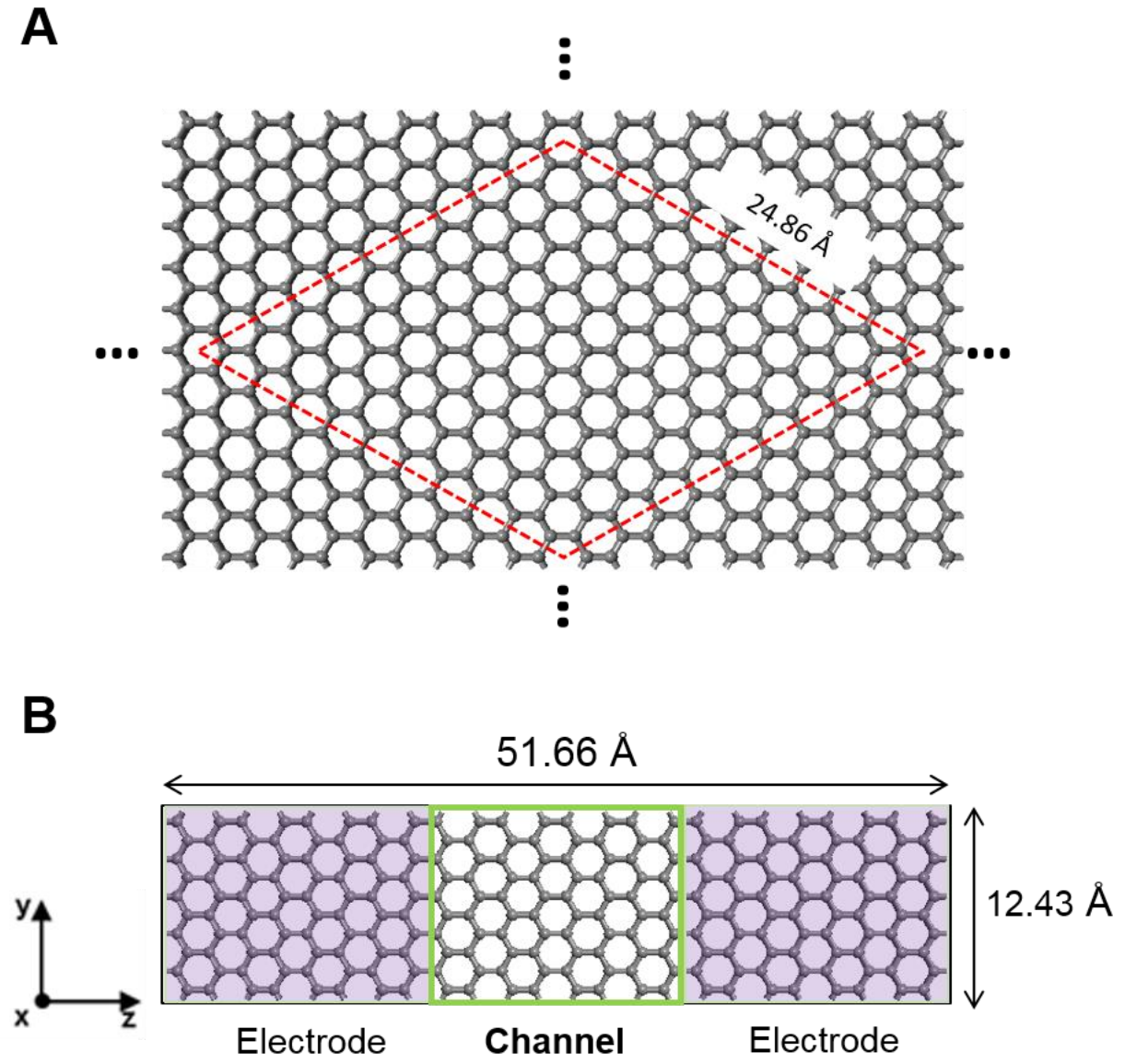

fig. S25. (A) Graphene models employed in DFT calculations. The 10 × 10 unit cell of graphene on which I^- or I_3^- is adsorbed is indicated in red dashed lines; **(B)** Computational setup for NEGF calculations. A total of 12 unit cells along the armchair dimer line direction was equally divided into left semi-infinite electrode, channel, and right electrode regions (4 unit cell-long each). Along the normal zigzag chain direction, six unit cells were adopted.

Adsorption geometries and energetics of I^- and I_3^- on the graphene basal plane. To model the realistic adsorption geometries, we considered three different representative adsorption sites (bridge, on-top, and hollow) of I^- and I_3^- relative to the carbon atoms within graphene (fig. S26). In the case of I_3^-, the molecules were placed parallel to graphene basal plane, and two different configurations (molecular axis along the armchair α and zigzag β directions) for each adsorption site were considered. Equilibrium interface models were constructed based on the adsorption energetics. The equilibrium adsorption distances d_{ad} were found to be in the range of 3.18 ~ 3.37 Å (3.18 ~ 3.25 Å for I^- and 3.31 ~ 3.37 Å for I_3^- cases), while adsorption energies E_{ad} were calculated to be in the range of –2.19 ~ –1.83 eV (–1.83 eV for I^- and –2.19 ~ –2.11 eV for I_3^- cases). While having a lower adsorption energy, the I^- adsorbent shows a shorter adsorption distance than its I_3^- counterpart. This implies that, with the I^- species, easier dynamic adsorption/desorption processes are available and a higher amount of charge transfer can be induced.

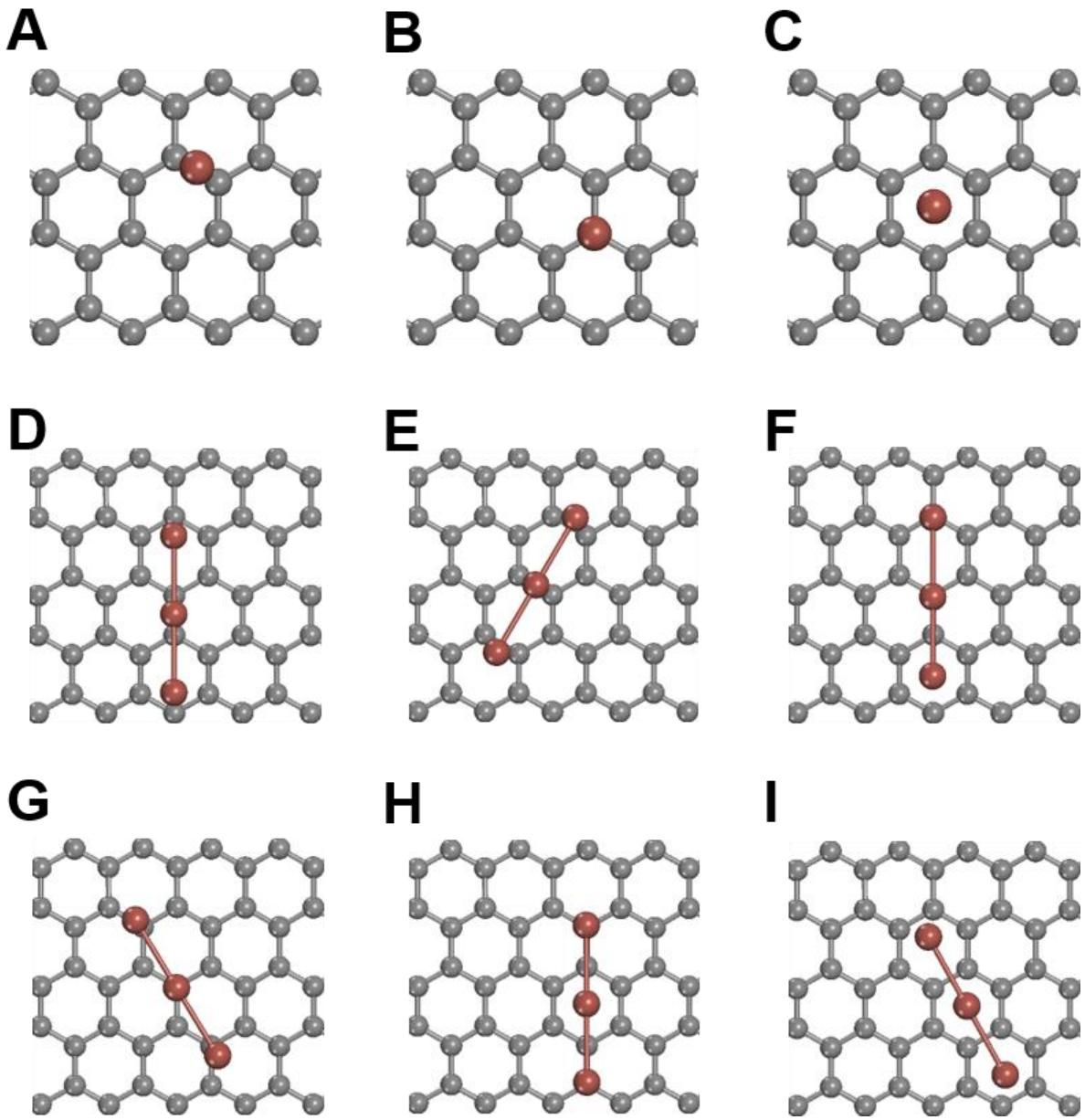

fig. S26. Configurations of I^- or I_3^- adsorbed on graphene. I^- at **(A)** Bridge (I^-_b); **(B)** On-top (I^-_o); **(C)** Hollow sites (I^-_h). I_3^- configurations were categorized in terms of the central I atom location (on the graphene bridge/on-top/hollow site) and the molecular axis alignment direction (along the graphene armchair/zigzag direction): (**D)** bridge-armchair (I_3^-_b_β); **(E)** bridge-zigzag (I_3^-_b_β); **(F)** on-top-armchair (I_3^-_o_α); **(G)** on-top-zigzag (I_3^-_o_β); **(H)** hollow-armchair (I_3^-_h_α); **(I)** hollow-zigzag (I_3^-_β).

Change in the electron population of graphene due to the I^-/I_3^- adsorption. Mulliken population analysis shows how the electrons are redistributed throughout the graphene basal plane with the adsorption of iodide and triiodide. As shown in fig. S27, for both I^- and I_3^- cases, charges of adsorbents will be transferred to graphene. More specifically, electrons are locally depleted around the adsorption site, and the small excess charges are distributed throughout the graphene basal plane. In other words, the adsorption of iodide and triiodide results in an effective electron doping of graphene, while inducing a localized hole doping around the adsorption site. Due to the difference in d_{ad} discussed in adsorption geometries and energetics of I^- and I_3^- on the graphene basal plane, the amount of charge transfer in the I^-/graphene interface (net charge of graphene ≈ –0.48 |e|) is higher than that in its I_3^-/graphene counterpart (net charge of graphene ≈ –0.22 |e|). In the case of transport models with a higher n_{I^-/I_3^-} = 0.47/nm^2 (compared with n_{I^-/I_3^-} = 0.19/nm^2 for DFT models), the amount of charge transfer was unexpectedly reduced to about – 0.39 |e| and – 0.13 |e| for the I^-/graphene and I_3^-/graphene interfaces, respectively. While seemingly counterintuitive, one can understand that this results from the reduction of graphene basal plane area that can accommodate the charge spill-over with the roughly fixed area of electron depletion next to the I^- or I_3^-.

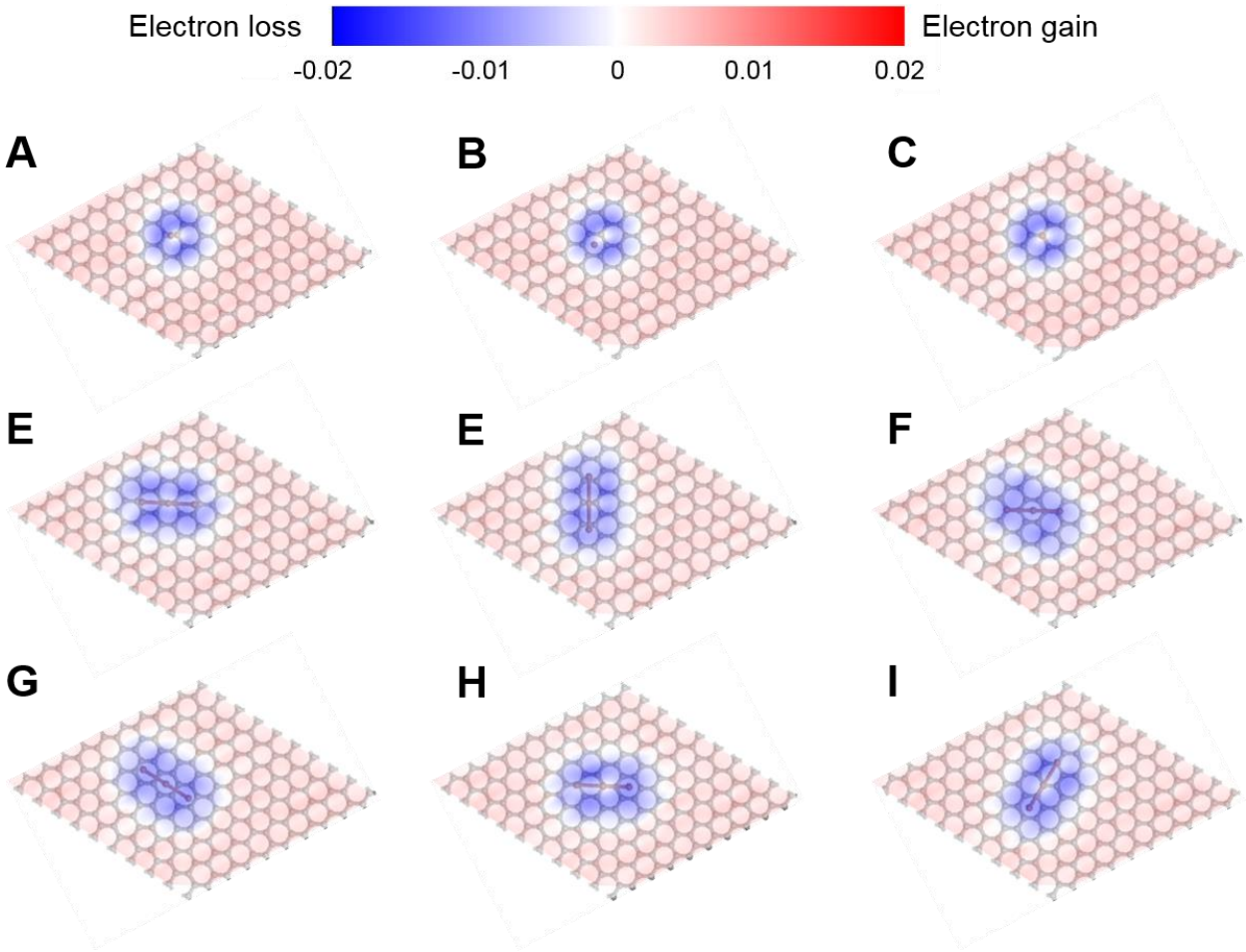

fig. S27. Mulliken charge populations in **(A)** I^-_b; **(B)** I^-_h**; (C)** I^-_o; **(D)** I_3^-_b_α; **(E)** I_3^-_b_β; **(F)** I_3^-_h_α; **(G)** I_3^-_h_β; **(H)** I_3^-_o_α; **(I)** I_3^-_o_β models (see fig. S26).

Modification in the transport properties of graphene due to the I^-/I_3^- adsorption. To investigate how the charge transport properties of graphene change with the adsorption of I^- and I_3^-, we have calculated the transmission the functions of all prepared I^-- and I_3^--adsorbed graphene models (fig. S28). While the impurity states of graphene originating from the I^-/I_3^- adsorption result in slight wiggling (peaks and dips), the overall shape of pristine graphene transmission function is well maintained. However, an n-type shift is evident, which results from the adsorbents-induced charge transfer between iodide (triiodide) and graphene discussed in the electron population change of graphene due to the I^-/I_3^- adsorption, and the corresponding upshift of E_F. Due to such effective electron doping, zero-bias electron transmission of graphene at E_F, $T(E_F)$, is noticeably enhanced up to 0.80 e^2/h for iodide and 0.0 ~ 0.40 e^2/h for triiodide cases, from the pristine graphene value of $T(E_F) = 0$. Note that the amount of E_F shift for the I^- case (–0.36 eV) is larger than that in the I_3^- case (0.0 ~ –0.08 eV), due to the difference in the amount of charge transfer described in the electron population change of graphene due to the I^-/I_3^- adsorption.

We finally calculated the *I*-*V* characteristics of graphene with the adsorption of iodide/triiodide according to Eq. 9, and the results are provided in fig. S28. In line with the transmission data, iodide cases show much enhanced currents than their triiodide counterparts (7.85 ~ 10.04 μA for the I^--adsorbed graphene vs. 1.71 ~ 2.94 μA for the I_3^--adsorbed graphene cases at 0.15 V, respectively).

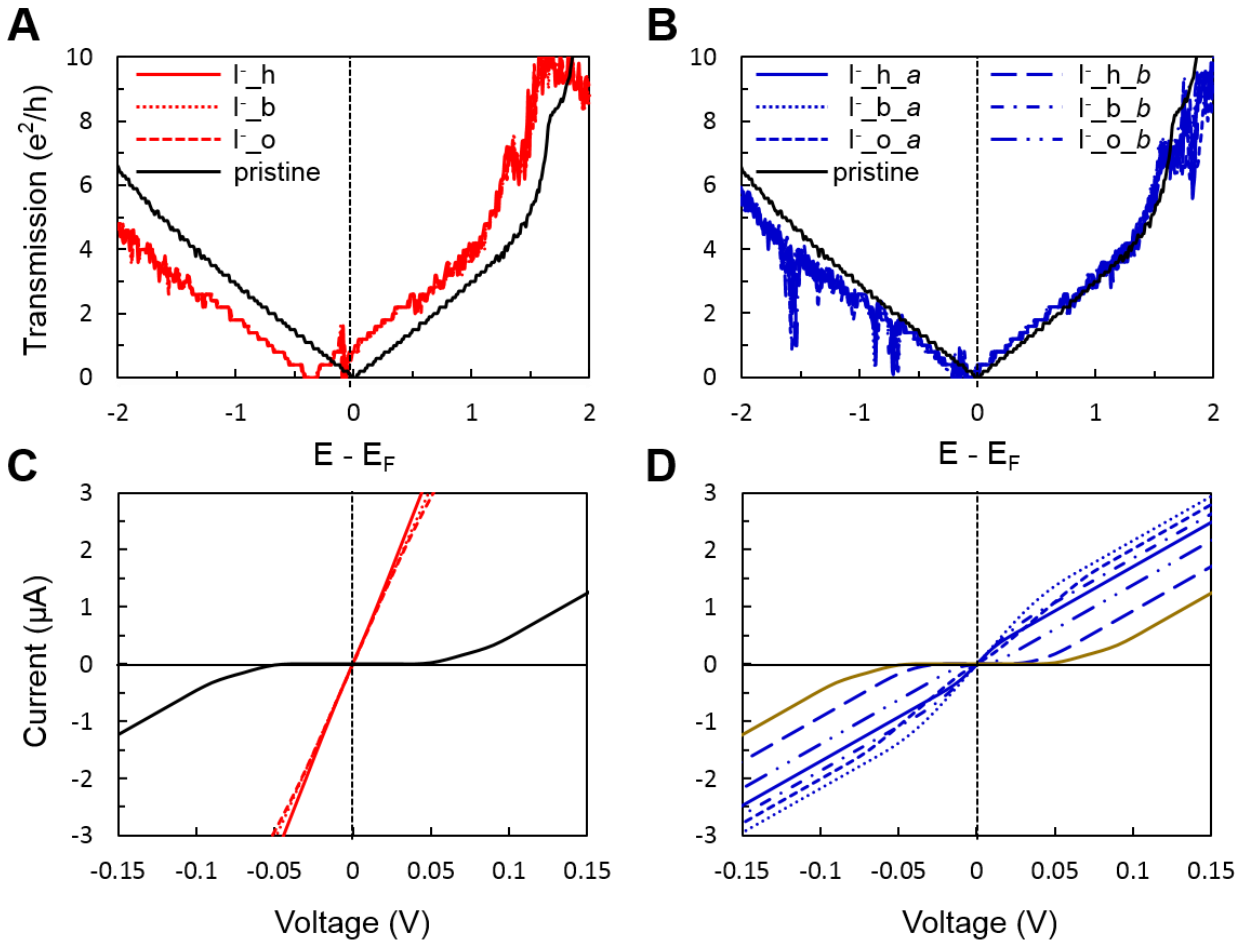

fig. S28. Transmission functions of graphene with different **(A)** I^- and **(B)** I_3^- adsorbent configurations (fig. S27) compared with the pristine graphene transmission function (black). Corresponding *I-V* characteristics of the **(C)** I^--adsorbed (red) and **(D)** I_3^--adsorbed (blue) graphene models compared with the pristine graphene *I-V* curve (black).

III. Additional Experimental Section

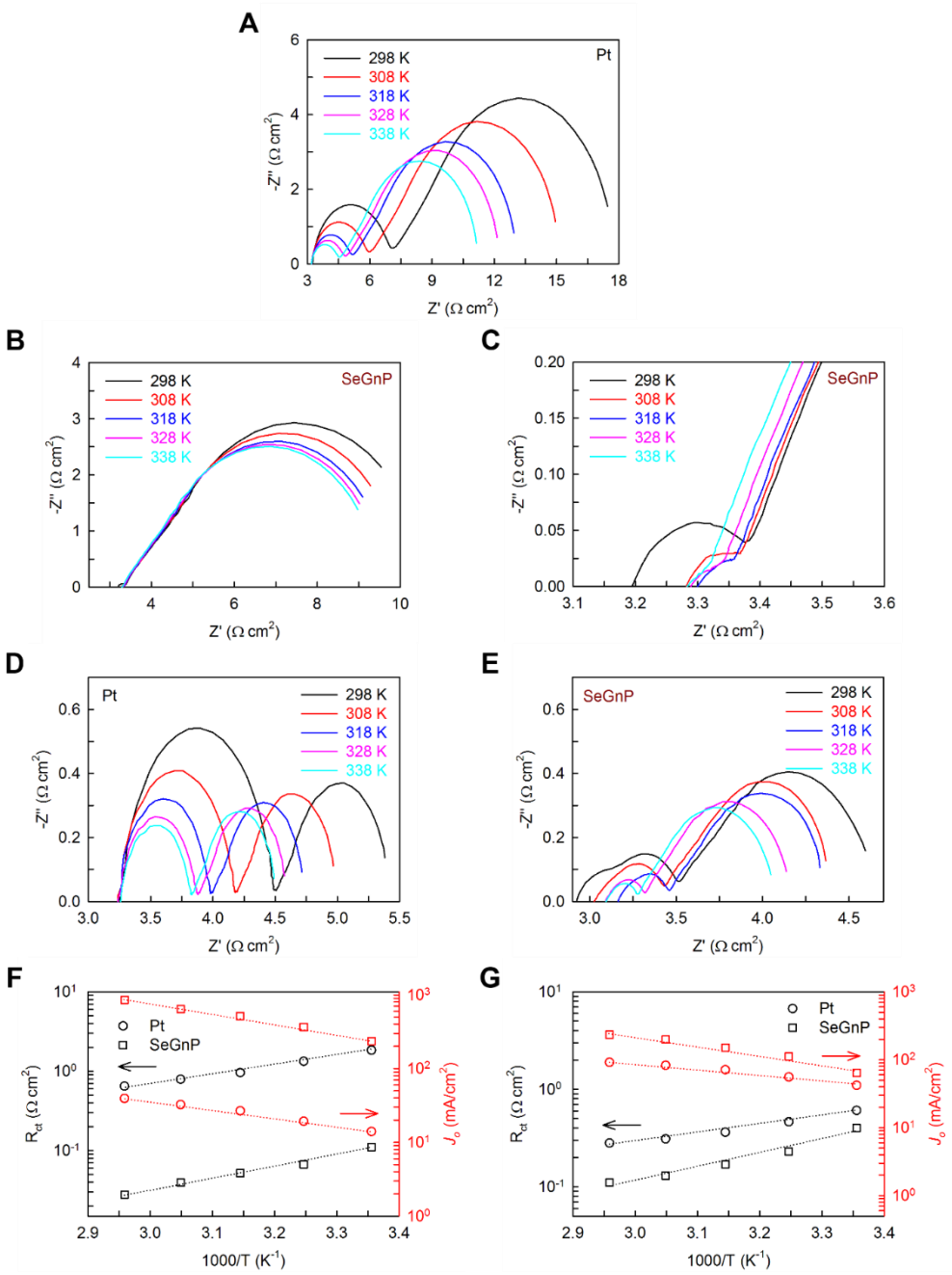

fig. S29. Nyquist plots obtained with $Co(bpy)_3^{2+/3+}$ and I^-/I_3^- electrolytes as a function of temperature: **(A)** Pt; **(B)** SeGnPs for $Co(bpy)_3^{2+/3+}$ electrolytes; **(C)** Enlarged Niquist plot at the high-frequency range in fig. S29B; **(D)** Pt; **(E)** SeGnPs for I^-/I_3^- electrolyte. Charge-transfer resistance-temperature and exchange current density-temperature data in Arrhenius plots with Pt- and SeGnP-CEs: **(F)** $Co(bpy)_3^{2+/3+}$; **(G)** I^-/I_3^-.

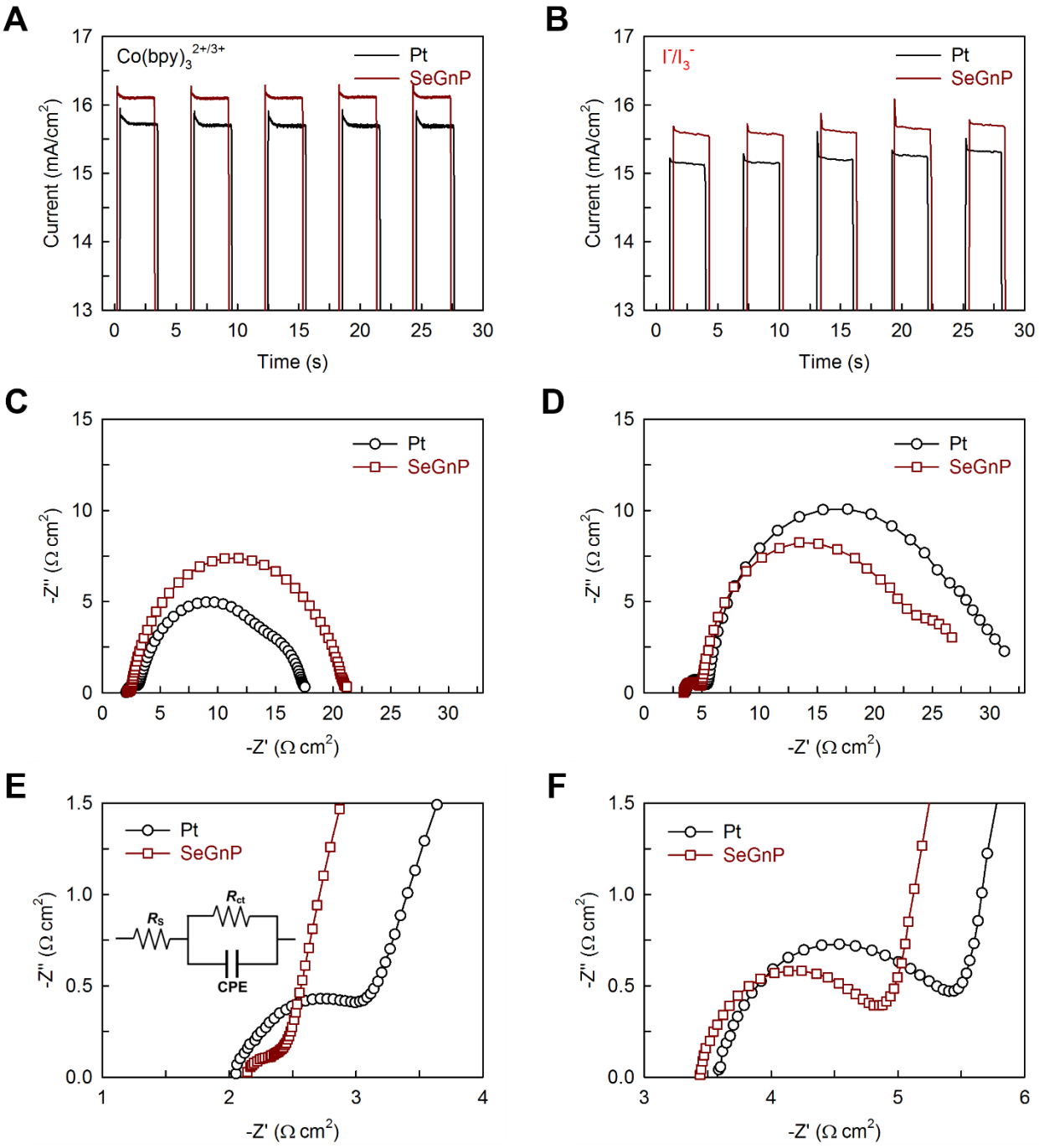

fig. S30. Photocurrent transient dynamics of the DSSCs: **(A)** SM315/Co(bpy)$_3^{2+/3+}$; **(B)** N719/I^-/I_3^-; Nyquist plots of the same DSSCs at applied bias; **(C)** –0.92 V; **(D)** –0.69 V under dark conditions; **(E)** and **(F)** enlarged Nyquist plots in the high-frequency regions of figs. S30C and S30D, respectively. The inset in fig. S30E is an EC for fitting the high-frequency region spectra.

Mass transport. The effect of mass transport of the $Co(bpy)_3^{2+/3+}$ and I^-/I_3^- redox couples in actual DSSCs with different CEs was investigated by monitoring photocurrent transients using a multi-step on/off modulation of the mass transfer limitation (figs. S30A and S30B). As can be seen, the ratio of the initial peak current to the steady state current in the photocurrent transients is almost consistent in the Pt- and SeGnP-DSSCs with $Co(bpy)_3^{2+/3+}$, while Pt- and SeGnP-DSSCs with I^-/I_3^- redox couple are significantly different. Considering that the DSSCs were fabricated under similar conditions, the mass transport of $Co(bpy)_3^{3+}$ and I_3^- ions in the pores of SeGnPs do not affect the overall cell efficiency.

To further understand the improved performance of the DSSCs with the SeGnP-CEs, EIS measurements were carried out on the DSSCs (figs. S30C and S30D). The first semicircles of the DSSCs with the SeGnP-CEs are somewhat smaller than those of the Pt-CEs. From the first semicircles, the R_{ct} values calculated by using the EC (inset in fig. S30E) on the DSSCs-SeGnP-CEs were 0.34 and 1.54 Ω cm^2 for the $Co(bpy)_3^{2+/3+}$ and I^-/I_3^- electrolytes, respectively, whereas the corresponding values of the DSSCs-Pt-CEs were 1.27 and 1.95 Ω cm^2. The lower R_{ct} values for the DSSCs with the SeGnP-CEs suggest higher electrocatalytic activities for the reduction of $Co(bpy)_3^{3+}$ and I_3^- ions than the Pt counterparts, which could enhance the DSSCs performance, in particular, *FF* and J_{sc} (Table 2).

table S1. TGA, EA, EDX, and XPS data of the pristine graphite and SeGnPs.

Sample	TGA (Char yield at 1000 °C)		Element	EA (wt.%)	EDX (at.%)	XPS (at.%)
	N_2	Air				
Graphite	99.1	23.7	C (%)	99.64	98.80	98.35
			O (%)	0.13	1.20	1.65
SeGnPs	75.8	0	C (%)	65.30	88.10	77.94
			O (%)	10.13	6.32	15.25
			H (%)	0.31	-	-
			Se (%)	24.26[a]	5.57	6.81

[a] Calculation from total wt.%

table S2. BET surface area, pore volume, and pore size of the pristine graphite and SeGnPs.

Sample	Surface Area (m^2 g^{-1})	Pore Volume (mL g^{-1})	Pore Size (nm)
Graphite	2.78	0.0016	2.27
SeGnPs	105.69	0.0687	2.60

table S3. The size of I_3^- and $Co(bpy)_3^{3+}$ions.

Ions	Diameter (Å)	Length (Å)
I_3^-	3.0	5.8
$Co(bpy)_3^{3+}$	4.7	9.5